# Implications of 3D Forest Stand Reconstruction Methods for Radiative Transfer Modeling: A Case Study in the Temperate Deciduous Forest

C. Liu, K. Calders, F. Meunier, J. P. Gastellu-Etchegorry, J. Nightingale, M. Disney, N. Origo, W. Woodgate, H. Verbeeck

▶ **To cite this version:**

C. Liu, K. Calders, F. Meunier, J. P. Gastellu-Etchegorry, J. Nightingale, et al.. Implications of 3D Forest Stand Reconstruction Methods for Radiative Transfer Modeling: A Case Study in the Temperate Deciduous Forest. Journal of Geophysical Research: Atmospheres, 2022, 127, pp.e2021JD036175. 10.1029/2021JD036175 . insu-03863709

**HAL Id: insu-03863709**
**https://insu.hal.science/insu-03863709**

Submitted on 16 Mar 2023

**HAL** is a multi-disciplinary open access archive for the deposit and dissemination of scientific research documents, whether they are published or not. The documents may come from teaching and research institutions in France or abroad, or from public or private research centers.

L'archive ouverte pluridisciplinaire **HAL**, est destinée au dépôt et à la diffusion de documents scientifiques de niveau recherche, publiés ou non, émanant des établissements d'enseignement et de recherche français ou étrangers, des laboratoires publics ou privés.

Copyright

Check for updates

JGR Atmospheres

RESEARCH ARTICLE
10.1029/2021JD036175

**Key Points:**

- The radiative transfer simulation bias of a voxelized versus spatially explicit canopy exceeds 5% in 81.6% of the simulations
- Voxelized objects reflected and absorbed less electromagnetic radiation than explicit objects: −45.6% in visible and −6% in NIR bands
- Voxel sizes 1–2 m are optimal for voxel-based radiative transfer simulations within the temperate deciduous forest studied

**Correspondence to:**
C. Liu,
Chang.Liu@UGent.be

**Citation:**
Liu, C., Calders, K., Meunier, F., Gastellu-Etchegorry, J. P., Nightingale, J., Disney, M., et al. (2022). Implications of 3D forest stand reconstruction methods for radiative transfer modeling: A case study in the temperate deciduous forest. *Journal of Geophysical Research: Atmospheres*, *127*, e2021JD036175. https://doi.org/10.1029/2021JD036175

Received 8 NOV 2021
Accepted 19 JUN 2022

© 2022. American Geophysical Union. All Rights Reserved.

# Implications of 3D Forest Stand Reconstruction Methods for Radiative Transfer Modeling: A Case Study in the Temperate Deciduous Forest

**C. Liu[1], K. Calders[1], F. Meunier[1], J. P. Gastellu-Etchegorry[2], J. Nightingale[3], M. Disney[4,5], N. Origo[4,6], W. Woodgate[7,8], and H. Verbeeck[1]**

[1]CAVELab - Computational & Applied Vegetation Ecology, Department of Environment, Ghent University, Ghent, Belgium, [2]Toulouse III University, CESBIO - CNES, CNRS, IRD, INRA Toulouse, Toulouse, France, [3]Climate Solutions Exchange Ltd, Richmond, UK, [4]Department of Geography, University College London, London, UK, [5]NERC National Centre for Earth Observation (NCEO), Leicester, UK, [6]Earth Observation, Climate and Optical Group, National Physical Laboratory, Teddington, UK, [7]School of Earth and Environmental Sciences, The University of Queensland, Brisbane, Australia, [8]Space and Astronomy, CSIRO, Kensington, WA, Australia

**Abstract** This study investigated the implications of different assumptions of 3D forest stand reconstructions for the accuracy and efficiency of radiative transfer (RT) modeling based on two highly detailed 3D stand representations: 3D-explicit and voxel-based. The discrete anisotropic radiative transfer (DART) model was used for RT simulations. The 3D-explicit and voxel-based 3D forest scenes were used as structural inputs for the DART model, respectively. Using the 3D-explicit RT simulation as the benchmark, the accuracy and efficiency of the voxel-based RT simulation were evaluated under multiple simulation conditions. The results showed that for voxel-based RT simulations: with voxel sizes 0.1, 1, and 10 m and in blue, green, red, and near-infrared wavebands, the normalized deviations of simulated directional reflectance exceeded the 5% tolerance limit in 89% viewing directions; with voxel sizes 0.2, 1, and 10 m, the normalized deviations of simulated spectral albedo exceeded the 5% tolerance limit in 90.5% wavelengths; for simulated spectral albedo in blue, green, red, and near-infrared wavebands and fraction of absorbed photosynthetically active radiation, the normalized deviations exceeded the 5% tolerance limit in 65.3% voxel sizes and spatial resolutions. The two major causes for differences in the 3D-explicit versus voxel-based RT simulations were: (a) the difference between light interaction in spatially explicit objects and in turbid medium, and (b) the structural difference of 3D contours between voxel-based and 3D-explicit models. However, voxel-based RT simulations were substantially more computationally efficient than 3D-explicit RT simulations in large voxel sizes (≥1 m) and coarse spatial resolutions (≥1 m).

## 1. Introduction

Remote sensing (RS) data can deliver spatially and temporally distributed information on Essential Climate Variables (Bojinski et al., 2014) in forest ecosystems. However, very few properties of interest for environmental applications can be measured directly by RS. Instead, they must be inferred from measurements of reflected, emitted, or scattered radiation using mathematical or empirical modeling, or via the proxy variable (e.g., vegetation indices) derived from the remotely sensed data. In this context, a proper understanding of the interaction between light (i.e., electromagnetic radiation) and forests is essential for vegetation RS interpretation and product development (Gastellu-Etchegorry et al., 2012).

Radiative transfer models (RTMs) are physically based models capable of simulating the interaction between light and forest structure (Widlowski et al., 2013, 2014). RTMs are useful for the forward modeling or inversion of key forestry RS products, for example, surface reflectance, albedo, and vegetation indices (VIs). Based on physical principles, the forward modeling simulates RS data from known parameters (e.g., forest structural information, leaf spectral properties, and solar irradiance data). In contrast, inverse modeling derives parameters of interest from RS data according to the same physical principles or an empirical relationship. Since the interaction between light and forests is an important part in RS observation, RTMs can help us better understand the physical principles of RS. Therefore, RTMs are of great significance for the calibration and validation of RS products. In addition, RTMs can provide information relevant to many key ecosystem processes such as photosynthesis and transpiration through detailed quantification of the light regime (scattering and absorption) within canopies.



21698996, 2022, 14, Downloaded from https://agupubs.onlinelibrary.wiley.com/doi/10.1029/2021JD036175 by Portail BibCNRS INSU, Wiley Online Library on [16/03/2023]. See the Terms and Conditions (https://onlinelibrary.wiley.com/terms-and-conditions) on Wiley Online Library for rules of use; OA articles are governed by the applicable Creative Commons License

21698996, 2022, 14, Downloaded from https://agupubs.onlinelibrary.wiley.com/doi/10.1029/2021JD036175 by Portail BibCNRS INSU, Wiley Online Library on [16/03/2023]. See the Terms and Conditions (https://onlinelibrary.wiley.com/terms-and-conditions) on Wiley Online Library for rules of use; OA articles are governed by the applicable Creative Commons License

The representation of forest structure is an essential input and impacts the performance of RTMs (Janoutová et al., 2019; Li et al., 2018; Van der Zande et al., 2011; Widlowski et al., 2014). A more accurate forest structure can be represented if fewer assumptions and approximations about physical quantities are used in the reconstruction process. RTMs with more accurate 3D forest structure representations result in more accurate radiative transfer (RT) simulations, and more physically realistic derived parameters in an inversion sense, which greatly improves RTMs' value in the calibration and validation of RS products. However, forest structure is highly complex. Accurate forest structure representation requires a tremendous amount of forest structural information (Åkerblom & Kaitaniemi, 2021; Disney, 2019; Widlowski et al., 2014). It requires the location, size, shape, and orientation of every single object in the canopy (e.g., leaf, branch, stem, etc.). It is also time and labor intensive, or even impossible to collect all this information by conventional methods (Åkerblom & Kaitaniemi, 2021; Disney, 2019). Thus, RTMs often simplify tree architecture to reduce the number of variables required to characterize the overall forest structure (Gobron et al., 1997; Kallel, 2010; Verhoef, 1984; Verhoef & Bach, 2007).

One-dimensional models such as PROSAIL (Jacquemoud et al., 2009) simulate RT using a spatially homogeneous canopy structure. Even in 3D RTMs, most studies use simple 3D geometries (e.g., ellipsoid or cone archetypes) to represent the 3D structure of trees (Cescatti, 1997; Kobayashi & Iwabuchi, 2008; Ni et al., 1999). The combination of these archetypes with the other inputs of the RTMs permits the generation of 3D scenes of different levels of complexity (Ebengo et al., 2021). Within-canopy clumping is typically not considered by crown archetypes. Thus, care is needed in inferring biophysical properties from these abstract representations (Calders et al., 2013; Schneider et al., 2014; Widlowski et al., 2014). A few studies generated detailed 3D tree structures according to the observed structural parameters and ecological properties (Disney et al., 2009, 2010, 2011; Stuckens et al., 2009; Woodgate et al., 2015). Such studies used field-measured parameters and parametric modeling of plant anatomy, topology, and growth to build explicit tree models using software like OnyxTree (www.onyxtree.com). The fourth phase of the radiative transfer model intercomparison (RAMI-IV) (Widlowski et al., 2015) used different 3D forest models. Individual trees were reconstructed using the xfrog (Lintermann & Deussen, 1999) or arbaro (Weber & Penn, 1995) software. The reconstruction was based on field inventory data or canopy information extracted from airborne laser scanning (ALS), thus limiting the detailed structural representation at finer scales (within crown and sub-branch).

The increased availability of terrestrial laser scanning (TLS) data offers a new way for highly accurate and realistic forest stand reconstruction (Åkerblom & Kaitaniemi, 2021; Calders et al., 2020; Disney, 2019). TLS is an active ground-based RS technology which acquires millimeter level of detail from the surrounding area (Liang et al., 2016). This allows rapid, automatic, and periodical measurement of forest structure. Based on the point cloud data obtained by TLS, highly detailed 3D forest models can be reconstructed and used as structural input in RTMs (Béland & Kobayashi, 2021; Calders et al., 2018; Cifuentes et al., 2018; Janoutová et al., 2019, 2021; Kükenbrink et al., 2021; Widlowski et al., 2014).

Voxel-based models and 3D-explicit models are two types of commonly used 3D forest models built from TLS data (Widlowski et al., 2014). The voxel-based model is made of cubes filled with a turbid medium. The turbid medium is an infinite number of infinitely small flat facets with specified angle distribution, area volume density ($m^2/m^3$), and spectral properties. These cubes are called voxels, which are 3D pixels in space. The voxel-based model is easier to parameterize and build than a fully 3D-explicit model. Because the area volume density of the turbid medium can be obtained from LiDAR data by calculating transmittance values using the Beer Lambert's turbid medium approximation (Vincent et al., 2017), or other methods utilizing contact frequency (Hosoi & Omasa, 2006). TLS can also successfully measure leaf angle with a range of approaches, including plane fitting (Hosoi & Omasa, 2015), grid triangulation (Bailey & Mahaffee, 2017), and full 3D estimation of surface normals (Vicari et al., 2019). RTMs with voxel-based structural input are also more computationally efficient (when voxel size is chosen appropriately). Thus, the voxel-based model is often used to construct large area (0.36–9 ha) 3D forest models from TLS and ALS data (Béland & Kobayashi, 2021; Kükenbrink et al., 2021; Schneider et al., 2014). However, the assumptions of a turbid medium to represent forest structure do not hold for clumped (spatially aggregated) objects like twigs, branches, and tree crowns. Therefore, the above assumptions and approximations of physical quantities within voxels can lead to a less accurate structural representation than the actual forest canopy.

3D-explicit models attempt to explicitly represent every tree's leaf, stem, and branch. Each object is reconstructed as a geometry similar to its shape and is assigned specific spectral properties. Therefore, the 3D-explicit

21698996, 2022, 14, Downloaded from https://agupubs.onlinelibrary.wiley.com/doi/10.1029/2021JD036175 by Portail BibCNRS INSU, Wiley Online Library on [16/03/2023]. See the Terms and Conditions (https://onlinelibrary.wiley.com/terms-and-conditions) on Wiley Online Library for rules of use; OA articles are governed by the applicable Creative Commons License

forest model uses fewer assumptions than the voxel-based model and has a more accurate and realistic structure. However, explicitly reconstructing every object in the forest stand requires a large amount of information and modeling work (Åkerblom & Kaitaniemi, 2021). The required information is difficult to measure and process. Moreover, RT modeling with a 3D-explicit model is normally computationally intensive. Only with the new Lux (bi-directional light propagation) mode of the discrete anisotropic radiative transfer (DART) model, the efficiency of RT modeling has been significantly improved (dozens of times faster than the DART flux-tracking mode depending on the complexity of the scene). Thus, few studies have reconstructed 3D-explicit forest models from TLS data including all trees within the forest stand, and even fewer have parameterized an RT model combining both structural and spectral scene properties. Some studies reconstructed 3D-explicit models of a few trees (less than five). These tree models were cloned multiple times to generate a forest stand, then used as input for the RTM (Côté et al., 2009; Janoutová et al., 2019; Widlowski et al., 2014). Some studies used simulated forest point cloud data or virtual tree models instead of in-situ scanned data (Li et al., 2018; Van der Zande et al., 2011). Only a few studies have reconstructed 3D-explicit scenes of large area forest stands for RTM purposes (Calders et al., 2016, 2018; Cifuentes et al., 2018).

We are now in a position to measure highly detailed 3D canopy structure routinely (Calders et al., 2020). But how to incorporate this structure into RTMs is not yet clear. The impact of different structural representations of highly detailed 3D forest reconstructions on RT modeling needs to be investigated and quantified. This study aimed to: (a) quantify the impact of 3D forest stand reconstructions (3D-explicit vs. voxel-based) on the accuracy and efficiency of RT modeling in a temperate deciduous forest; and (b) provide guidance for choosing the appropriate 3D forest model for RTMs in a temperate deciduous forest. This study conducted RT modeling using two highly detailed 3D model representations (3D-explicit and voxel-based models) of a 1-ha temperate deciduous forest (Calders et al., 2018). Using the 3D-explicit RT simulation as the benchmark, the accuracy of the voxel-based RT simulation was evaluated under multiple experimental conditions, and the reasons for the deviations were analyzed. The efficiency of running the RTMs with various 3D models, that is, time and resource consumption, was also evaluated.

## 2. Materials and Methods

### 2.1. Study Area and Data Collection

The study site is a mixed deciduous forest located in Wytham Woods, UK. Wytham Woods is a typical temperate forest site in southern Great Britain (Kirby et al., 2014; Savill et al., 2011). The study area is nested within an 18-ha long-term forest inventory plot run by Oxford University and is part of the ForestGEO global network of forest inventory plots (Calders et al., 2018). The mean annual temperature and rainfall are 10°C and 729 mm, respectively. Sycamore (*Acer pseudoplatanus*), common ash (*Fraxinus excelsior*), and common hazel (*Corylus avellana*) are the dominant tree species in the study area.

The study was conducted on a 1-ha forest plot (100 × 100 m). All the 550 trees in the plot were used in the study. There were six tree species, with 520 live trees all having leaves, and 30 trees were dead standing. 3D structural data of trees and a digital elevation model (DEM) were collected by a RIEGL VZ-400 terrestrial laser scanner. The spectral properties of the leaves and bark of each tree species, and understorey were collected using a FieldSpec (ASD Spectrometer). An ASD leaf clip and plant probe attached to the ASD Spectrometer were used to measure the leaf reflectance. The leaf transmittance was extrapolated using the PROSPECT model and the measured reflectance data. The ASD contact probe attachment was used to measure the spectral properties of the bark. The bare fiber and pistol grip attachment of ASD Spectrometer were used to measure the understorey reflectance. The 1-ha plot was divided into 25 grids of 20 × 20 m. In the middle of each grid, the understorey reflectance of five samples was measured. And their average formed the final representative spectral measurement of this grid. For every five grids, a white reference panel measurement was taken. The final understorey reflectance was the average value of all grids. A detailed description of the data collection can be found in Calders et al. (2018).

### 2.2. Three-Dimensional Forest Stand Reconstruction

#### 2.2.1. 3D-Explicit Model

The Wytham Woods 3D model (Calders et al., 2018) was used as the 3D-explicit model in this study. The Wytham Woods model represents a 3D model of a 1-ha forest plot. Every tree was explicitly built in the Wytham

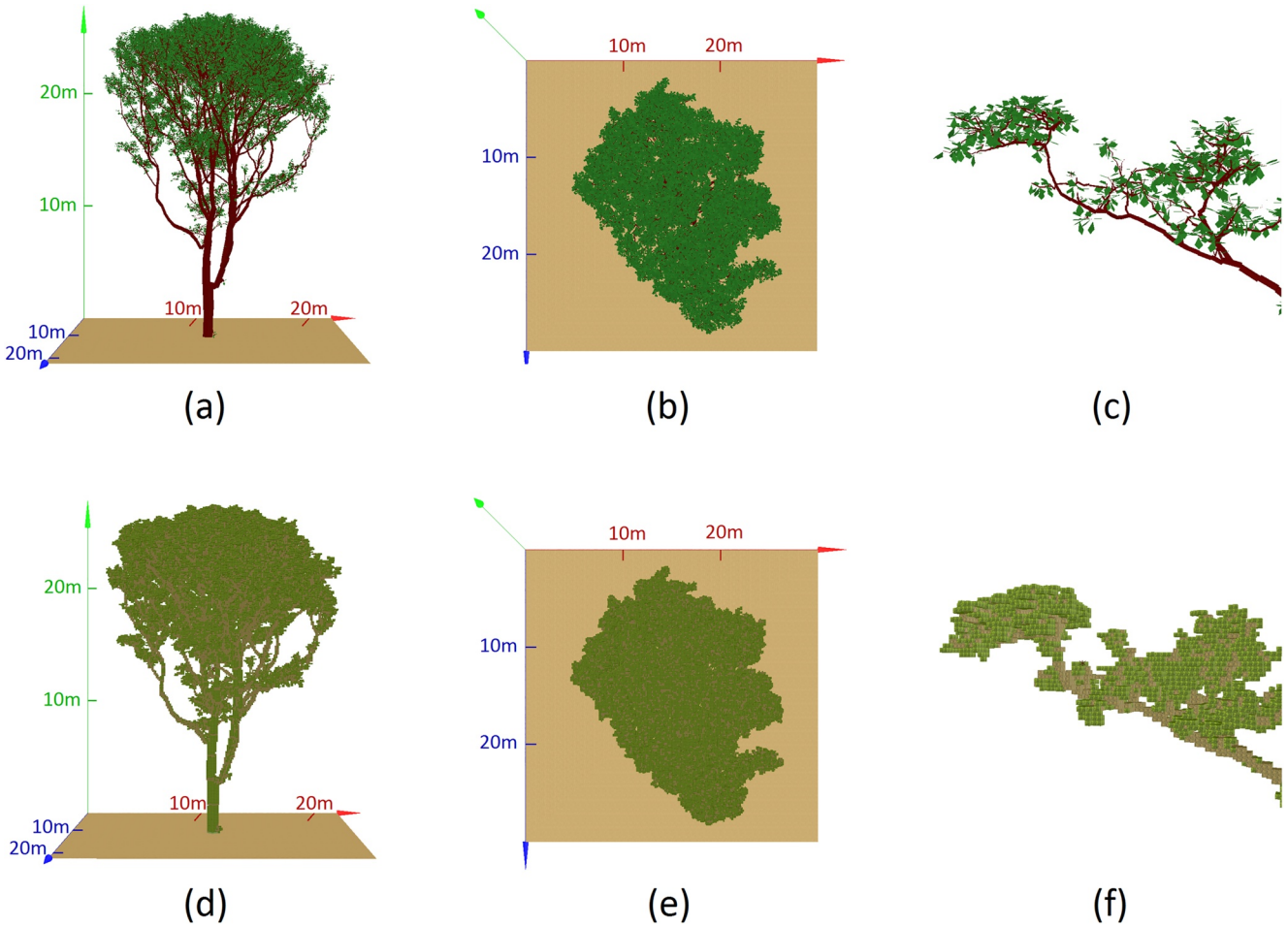


**Figure 1.** The 3D-explicit model (top row) and voxel-based model (bottom row) of a single tree. (Left): front view; (middle): top view; (right): model details of branches and leaves. Voxel size: 0.1 m. The voxels use different colors for enhanced visualization.

Woods 3D model. The model was made of solid facets with similar shapes and sizes to real objects. Every branch and stem was individually reconstructed using quantitative structural models (QSMs) (Calders et al., 2015; Hackenberg et al., 2015; Juchheim et al., 2017) based on the 3D structural data obtained by TLS. The leaves were added to the tree QSM structure using the Foliage and Needles Naïve Insertion (FaNNI) algorithm (Åkerblom et al., 2018) to generate the 3D-explicit model of the single tree (Figures 1a–1c). The spectral properties of every leaf, stem, and branch were assigned according to the tree species and the in-situ measured spectral data (Figure 2). Finally, the 3D-explicit forest model was constructed by combining all the 3D tree models and DEM (Figure 3a, Figure A1). A detailed description of the Wytham Woods 3D-explicit model can be found in Calders et al. (2018). We chose the Wytham Woods 3D-explicit model for this study because this model is, to our knowledge, the most explicitly modeled real forest to date. Additionally, the reconstruction framework of the 3D model is generic, highly transferable, and adjustable to data collected with other TLS instruments and different ecosystems (Calders et al., 2018).

### 2.2.2. Voxel-Based Model

The voxel-based 3D model (Figures 1d–1f, 3b, Figure A2) was built from the 3D-explicit model using the DART software (Gastellu-Etchegorry et al., 2012). The objects of the 3D-explicit model, that is, the solid facets, were transformed into voxels. The voxel is a cube filled with "turbid medium" inside, which is a statistical representation of vegetation: each voxel is filled with an infinite number of infinitely small flat facets. The turbid medium is characterized by three properties: plant area index (PAI), plant angle distribution (PAD), and spectral properties



21698996, 2022, 14, Downloaded from https://agupubs.onlinelibrary.wiley.com/doi/10.1029/2021JD036175 by Portail BibCNRS INSU, Wiley Online Library on [16/03/2023]. See the Terms and Conditions (https://onlinelibrary.wiley.com/terms-and-conditions) on Wiley Online Library for rules of use; OA articles are governed by the applicable Creative Commons License

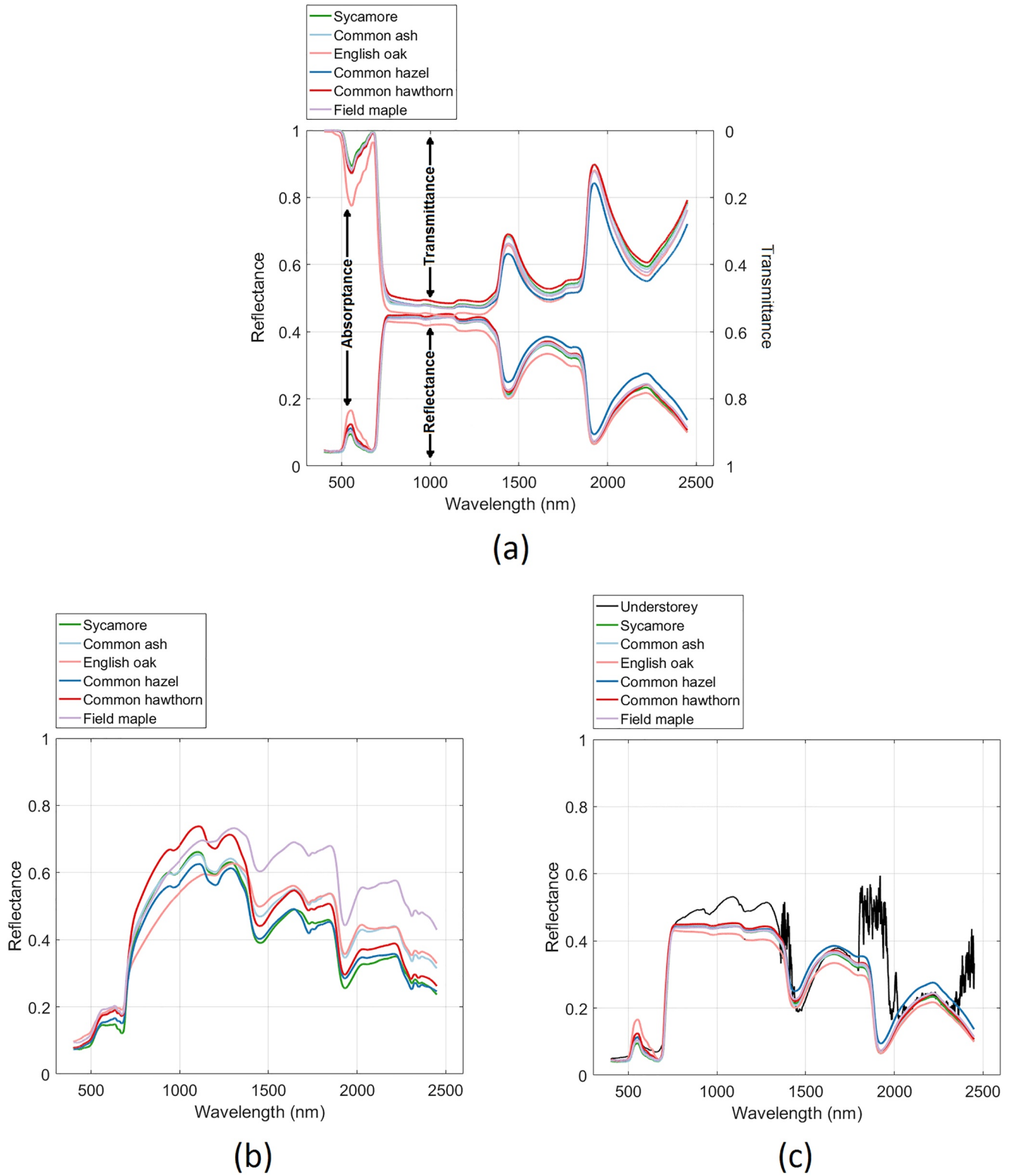


**Figure 2.** Spectral properties of different tree species. (a) Reflectance and transmittance of leaves. (b) Reflectance of bark. (c) Reflectance of understorey (black), together with reflectance of leaves as a comparison.



21698996, 2022, 14, Downloaded from https://agupubs.onlinelibrary.wiley.com/doi/10.1029/2021JD036175 by Portail BibCNRS INSU, Wiley Online Library on [16/03/2023]. See the Terms and Conditions (https://onlinelibrary.wiley.com/terms-and-conditions) on Wiley Online Library for rules of use; OA articles are governed by the applicable Creative Commons License

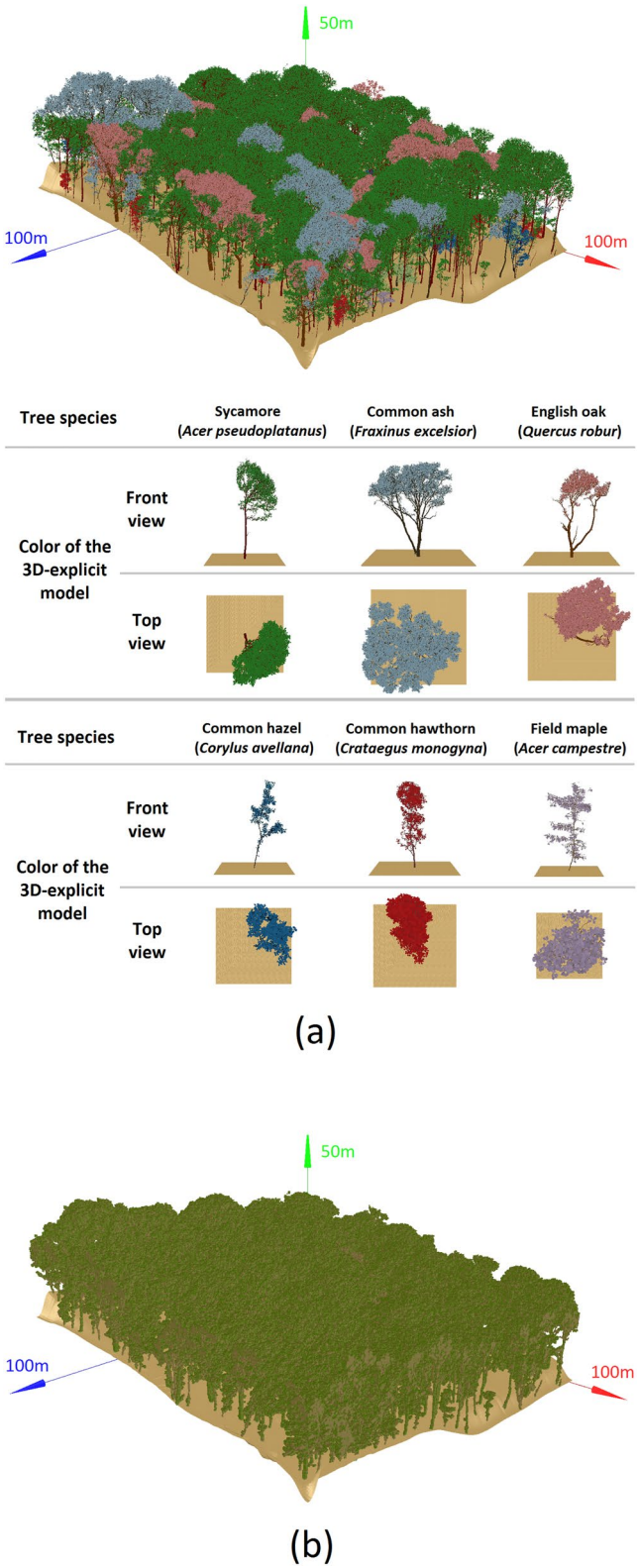


**Figure 3.** (a) The 3D-explicit model of the 1-ha forest plot. The different colors represent the different tree species present in Wytham Woods. (b) The voxel-based model of the 1-ha forest plot. Voxel size: 0.2 m.

(reflectance, transmittance, and absorptance). These properties determine the density, orientation, and spectral properties of the infinitely small flat facets in the voxel.

The PAI and PAD of each voxel were calculated based on the solid facets of the 3D-explicit model located inside the voxel position. The PAI value was equal to the solid facets' total one-sided surface area within the voxel. The PAD was derived from the solid facets' orientations within the voxel. A detailed description of the PAD calculation method can be found in Gastellu-Etchegorry (2021). The spectral properties of the turbid medium were the same as that of the solid facets within the voxel. Since there were multiple tree species and both leaf and woody components in the scene, voxels in this study are treated as "mixed" voxels. In each voxel, the objects were transformed into turbid medium separately according to their tree species and component type (leaf or wood). Then these turbid mediums constituted a "mixed" voxel. The voxel has multiple types of turbid mediums inside, and each turbid medium has its own properties. In the RT simulation, the light is intercepted (absorbed, reflected, or transmitted) by the voxel for incident light along a direction. The transfer function describes the angular distribution of light intensity after this interception. The transfer function of the voxel was calculated according to the proportions and properties of all the turbid medium inside the voxel. Finally, the transfer function of each voxel was used for the RT simulation of the whole scene.

This study built the voxel-based model directly from the 3D-explicit model. This ensures that the voxel-based model's parameterization was the same as the 3D-explicit model. In other words, the PAI, PAD, and spectral properties of the turbid medium inside each voxel are the same as the objects of the 3D-explicit model at the same location. This is important for accurately and quantitatively comparing and describing the difference between 3D-explicit and voxel-based RT simulations.

### 2.3. Radiative Transfer Modeling

The DART model (Gastellu-Etchegorry, 2008; Gastellu-Etchegorry et al., 1996, 2004, 2012) was used for RT simulations in this study. The DART model allows both voxelized and explicit representations of 3D structure that can be driven by measured structure. The DART model is one of the most comprehensive physically based 3D models simulating the Earth-atmosphere radiation interaction from visible to thermal infrared wavelengths. It also has been comprehensively benchmarked for simulating vegetation canopy reflectance against other RTMs (Widlowski et al., 2015).

The 3D-explicit and voxel-based 3D forest scenes were used as structural inputs for the DART model, respectively. The same spectral properties were allocated to the two 3D models according to the species of each tree (Figure 2). The 3D forest scene was replicated around itself to become a horizontally infinite repetitive scene to ensure energy conservation. During the replication, the altitude of DEM's edge was slightly shifted to ensure the continuity of topography and scene. A detailed description of the scene replication can be found in Gastellu-Etchegorry (2021) (see "infinite slope").

To comprehensively understand the performance of different structural representations of forest structure on RTMs, simulations were conducted multiple times under different simulation conditions, that is, in different wavelengths, view geometry, voxel sizes, and spatial resolutions. The



21698996, 2022, 14, Downloaded from https://agupubs.onlinelibrary.wiley.com/doi/10.1029/2021JD036175 by Portail BibCNRS INSU, Wiley Online Library on [16/03/2023]. See the Terms and Conditions (https://onlinelibrary.wiley.com/terms-and-conditions) on Wiley Online Library for rules of use; OA articles are governed by the applicable Creative Commons License

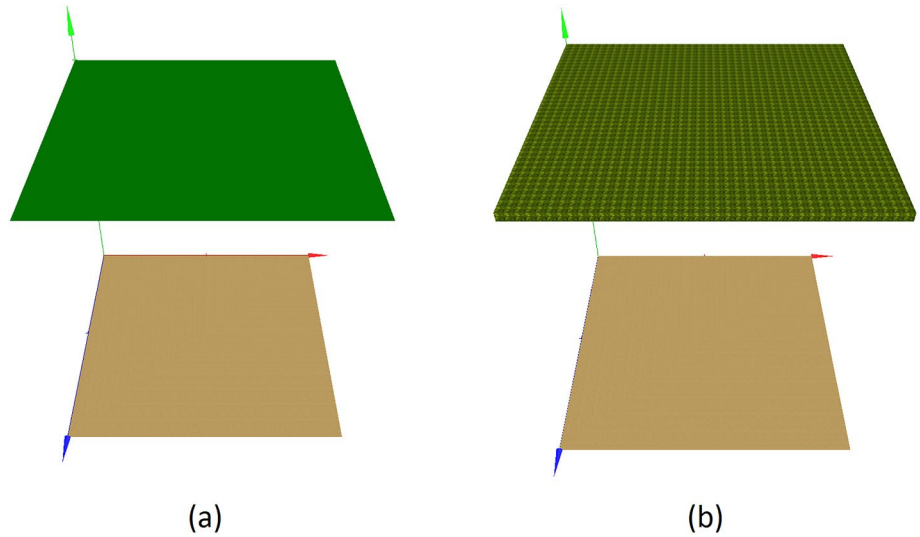


**Figure 4.** Illustration of the single-layer radiative budget experiments. A 3D-explicit facet (a) and a single-layer turbid medium (voxelized facet) (b) with the same PAI, PAD, and spectral properties were compared for their differences in reflectance, absorptance, and transmittance. The voxelized layer has a width of 1 m. The experiments were conducted in cyclic boundary conditions to ensure energy conservation (i.e., the 3D-explicit object, voxelized layer, and the scene are all horizontally infinite). The single-layer object was placed 20 m above the ground.

wavelength ranged from 400 to 2,450 nm, separated into 55 wavebands. Thirteen of the wavebands matched those of the Sentinel-2 satellite. The other 42 wavebands were hyperspectral wavebands. The first band began at 400 nm and the last band centered at 2,450 nm (50 nm step size and 5 nm bandwidth). The voxel size and spatial resolutions ranged from 0.1 to 50 m, with intermediary values of 0.2, 0.25, 0.275, 0.3, 0.35, 0.5, 1, 2, 5, 10, and 20 m. These values matched the spatial resolutions of current RS sensors (e.g., Sentinel-2, ICESat-2, and Planet). The viewing zenith angle (VZA) ranged from 0° to 90° and all the viewing azimuth angles (VAA) were used (0°–360°). In all the simulations, the solar zenith angle was set at 30° and the solar azimuth angle was set at 101° (DART coordinate system), which was the same as Calders et al. (2018).

To better investigate the fundamentals that cause the differences between 3D-explicit and voxel-based RT simulations, we documented the RT simulation differences between 3D-explicit and turbid medium 3D representations in the absence of 3D contour structure differences. To this end, we simulated the spatial light distribution (radiative budget) of two scenes. Both scenes only had a single-layer object and ground (Figure 4). More specifically, one scene used a 3D-explicit object, that is, a facet. The other scene voxelized the object and had a single-layer turbid medium, that is, a facet made of voxels (Figure 4). The spectral characteristics of the 3D-explicit object and the turbid medium inside the voxel were the same. The spectral properties of the most dominant tree species, sycamore, were used in this single-layer experiment. We used a vertical solar condition for this single-layer experiment: solar zenith angle 0°. The width of the voxelized layer was 1 m. The experiments were conducted with cyclic boundary conditions to ensure energy conservation. Hence the 3D-explicit object, voxelized layer, and the scene were all horizontally infinite. The single-layer object was placed 20 m above the ground. This height was similar to the canopy height. The single-layer experiment was conducted in blue, green, red, and NIR wavebands (490 ± 65, 560 ± 35, 665 ± 30, and 842 ± 115 nm).

### 2.4. Evaluation Method

The 3D-explicit RT simulation was used as the benchmark for the accuracy evaluation of voxel-based RT simulation. The results of voxel-based RT simulation were compared with those of 3D-explicit RT simulation to quantify its simulation deviation. The simulation settings were the same for both simulations except for the structural input (i.e., the 3D forest model).

Surface reflectance ($\rho_s$), directional reflectance ($\rho_d$), spectral albedo, and VIs were simulated in the top of canopy (TOC) simulations. The radiative budget (RB) simulations simulated the fraction of absorbed photosynthetically



21698996, 2022, 14, Downloaded from https://agupubs.onlinelibrary.wiley.com/doi/10.1029/2021JD036175 by Portail BibCNRS INSU, Wiley Online Library on [16/03/2023]. See the Terms and Conditions (https://onlinelibrary.wiley.com/terms-and-conditions) on Wiley Online Library for rules of use; OA articles are governed by the applicable Creative Commons License

21698996, 2022, 14, Downloaded from https://agupubs.onlinelibrary.wiley.com/doi/10.1029/2021JD036175 by Portail BibCNRS INSU, Wiley Online Library on [16/03/2023]. See the Terms and Conditions (https://onlinelibrary.wiley.com/terms-and-conditions) on Wiley Online Library for rules of use; OA articles are governed by the applicable Creative Commons License

active radiation (FAPAR). TOC and RB simulations are RT simulations with different outputs. The definition of TOC simulation and RB simulation are explained in detail in Nomenclature. These simulated parameters were used to evaluate the accuracy of the voxel-based RT simulation. Surface reflectance here is defined as the ratio of reflected radiant flux from the surface to the reflected radiant flux from an ideal diffuse reference panel for specific incidents or viewing cases. Directional reflectance is the mean surface reflectance of the whole scene in a specific viewing direction. Spectral albedo is the ratio between the reflected energy and the incident energy over the scene in a specific waveband. It is the integral of reflectance weighted by incident flux over hemispheric viewing directions ($2\pi$). VIs are usually obtained by linear or nonlinear combination operations on remotely sensed reflectance data of multiple wavebands, which are simple and effective parameters for characterizing vegetation cover and growth status (Liang & Wang, 2020). The deviation of simulated VIs could show the accuracy of voxel-based RT simulation on the aspect of practical RS applications. The normalized difference vegetation index (NDVI) and enhanced vegetation index (EVI) (Fang & Liang, 2008) were simulated in this study as common proxies of vegetation abundance and vigor. They are respectively defined as:

$$\mathrm{NDVI} = \frac{\rho_{\mathrm{NIR}} - \rho_{\mathrm{RED}}}{\rho_{\mathrm{NIR}} + \rho_{\mathrm{RED}}} \tag{1}$$

$$\mathrm{EVI} = 2.5 \times \frac{\rho_{\mathrm{NIR}} - \rho_{\mathrm{RED}}}{\rho_{\mathrm{NIR}} + 6 \times \rho_{\mathrm{RED}} - 7.5 \times \rho_{\mathrm{BLUE}} + 1} \tag{2}$$

where $\rho_{\mathrm{NIR}}$, $\rho_{\mathrm{RED}}$, and $\rho_{\mathrm{BLUE}}$ are the reflectance in near-infrared (NIR), red, and blue wavebands. These wavebands are based on RGB and NIR bands from the MSI instrument on Sentinel-2. The FAPAR is the ratio of the absorbed photosynthetically active radiation (PAR) in the spectral range of 400–700 nm to the total PAR that arrives at the top of the canopy. FAPAR is commonly used in ecosystem models (Liu et al., 2018).

The deviation of the voxel-based RT simulation was evaluated using normalized deviations of simulated $\rho_s$, $\rho_d$, spectral albedo, VIs, and FAPAR. For $\rho_d$, spectral albedo, VIs, and FAPAR, the normalized deviation ($D$) were calculated as:

$$D = \frac{v - r}{r} \tag{3}$$

where $v$ and $r$ are simulated values from voxel-based and 3D-explicit RT simulations, respectively.

For $\rho_s$, each pixel's normalized deviation and the absolute normalized deviation were calculated using Equations 4 and 5, respectively.

$$D_{(i,j)} = \frac{v_{(i,j)} - r_{(i,j)}}{\frac{1}{m \times n} \times \sum_{i=1}^{m} \sum_{j=1}^{n} r_{(i,j)}} \tag{4}$$

$$|D_{(i,j)}| = \frac{|v_{(i,j)} - r_{(i,j)}|}{\frac{1}{m \times n} \times \sum_{i=1}^{m} \sum_{j=1}^{n} r_{(i,j)}} \tag{5}$$

$v_{(i,j)}$ and $r_{(i,j)}$ are simulated surface reflectance values at pixel location $(i, j)$, from voxel-based and 3D-explicit RT simulations, respectively. $m$ and $n$ are the numbers of pixel rows and columns of the simulated reflectance image.

The typical uncertainty associated with vicarious calibration efforts of satellite observations (e.g., Bruegge et al., 2002; Kneubuhler et al., 2002; Thome, 2001; Thome et al., 2008; Wang et al., 2011) was used as the tolerance criteria for the simulated results. More specifically, an upper tolerance level of 5% was used. The simulations were deemed valid if their deviation fell within the 5% tolerance level.

The time and RAM consumption of RT simulations were used to evaluate the computational efficiency of RTMs. Since the TOC and RB simulations of RT modeling were conducted separately, the sum of their consumption was used for the efficiency evaluation. The RT simulations were conducted at the HPC facility of Ghent University. The hardware and simulation settings related to efficiency are listed in Table 1.

21698996, 2022, 14, Downloaded from https://agupubs.onlinelibrary.wiley.com/doi/10.1029/2021JD036175 by Portail BibCNRS INSU, Wiley Online Library on [16/03/2023]. See the Terms and Conditions (https://onlinelibrary.wiley.com/terms-and-conditions) on Wiley Online Library for rules of use; OA articles are governed by the applicable Creative Commons License

**Table 1**
*Hardware Condition and Simulation Settings Related to Efficiency*

| | | |
|---|---|---|
| Hardware | Intel Xeon Gold 6240 (Cascade Lake@ 2.6 GHz, useable RAM: 738 GiB) one node × 18 processors for each RT simulation (one node × 36 processors for voxel-based RT simulation with voxel size 0.1 m) | |
| DART simulation settings | Radiative method | Flux-tracking |
| | Number of directions | 129 |
| | Number of wavebands | 55 |
| | Smaller mesh size *D* of BOA irradiance sources | 0.01 m |
| | Image options: spreading or rays | Precise (slow) |

## 3. Results and Discussion

### 3.1. Deviation of Voxel-Based Radiative Transfer Simulation

#### 3.1.1. Spatial Patterns of Surface Reflectance Deviation

Nadir images of the voxel-based RT simulation had lower $\rho_s$ than the 3D-explicit RT simulation (Figures 5 and 6). The mean $\rho_s$ of the voxel-based images were 5.7%–37.4% lower than 3D-explicit images, depending on the wavebands and the voxel sizes (Table 2). There was only one exception, in the red waveband and voxel size 10 m, where the mean $\rho_s$ of the voxel-based image were 12.4% higher than the 3D-explicit image. This positive peaked value is due to more light reaching the understorey with a larger voxel size, and the understorey reflects much more light than the canopy in the red waveband.

More specifically, for the red waveband, the reflectance difference between understorey and leaves is much higher than in blue, green, and NIR wavebands because understorey reflectance is 1.5 times greater than the highest leaf reflectance in the red waveband (0.070 vs. 0.047, Figure 2c). While for the blue, green, and NIR wavebands, understorey reflectance is 1.2, 0.7, and 1.1 times higher than the highest leaf reflectance, respectively. Therefore, the understorey reflected much more light than the canopy in the red waveband. Also, for the larger voxel sizes, there are fewer gaps inside and under the canopy in the voxel-based model, and the scene's height is also higher. From the whole scene perspective, this means that the objects are less clumped, distributed over a larger space, and more evenly distributed. Compared with the structure in smaller voxel sizes, this structure causes more light to reach the understorey. Combining the above two reasons, more light reached the understorey in larger voxel sizes, and the understorey reflected much more light than the canopy in the red waveband. Therefore, the voxelized scene reflected more light to the sensor in the red waveband and with a voxel size of 10 m, compared to other wavebands and smaller voxel sizes. Its normalized deviation is higher and there is a positive peaked value.

For the distribution of pixel $\rho_s$ values, the standard deviation of voxel-based images was lower than 3D-explicit images. The distribution ranges of pixel $\rho_s$ were smaller in voxel-based images (Figure 6), and the $\rho_s$ difference between adjacent pixels was smaller (Figure 5). The above trends were also valid for the NIR waveband (Figures A3 and A4).

Due to the adopted species-specific leaf spectral properties, the $\rho_s$ differences between 3D-explicit and voxel-based models were amplified. With the 0.1 m voxel size, the normalized $\rho_s$ deviation change rate was basically the same as the rate of the leaf reflectance change. There are three dominant tree species in this experimental scene: sycamore (*Acer pseudoplatanus*), common ash (*Fraxinus excelsior*), and English oak (*Quercus robur*). The reflectance of English oak leaves in the green waveband is 1.78 times that of sycamore and 1.65 times that of common ash. This tree species had a higher $\rho_s$ deviation in the green band, and the color is greener in the deviation RGB map (Figures 5c, 5f). With the 0.1 m voxel size, its absolute normalized $\rho_s$ deviation in the green waveband was 1.75 times that of sycamore and 1.72 times that of common ash (83% vs. 47.3% and 48.2%), which was approximately the same as the multiples in reflectance change. This trend also applied to the red, blue, and NIR wavebands (Table 3).

To better understand the reasons for the $\rho_s$ deviation of the voxel-based RT simulation, the positive and negative $\rho_s$ deviations were separated for further analysis (Figure 7). According to the objects located in the pixel, the image pixels can be classified into four types: canopy pixels, canopy gap pixels, pixels of pure woody components (isolated dead trees, referred to as "pure-wood"), and pixels of the ground under the pure woody components

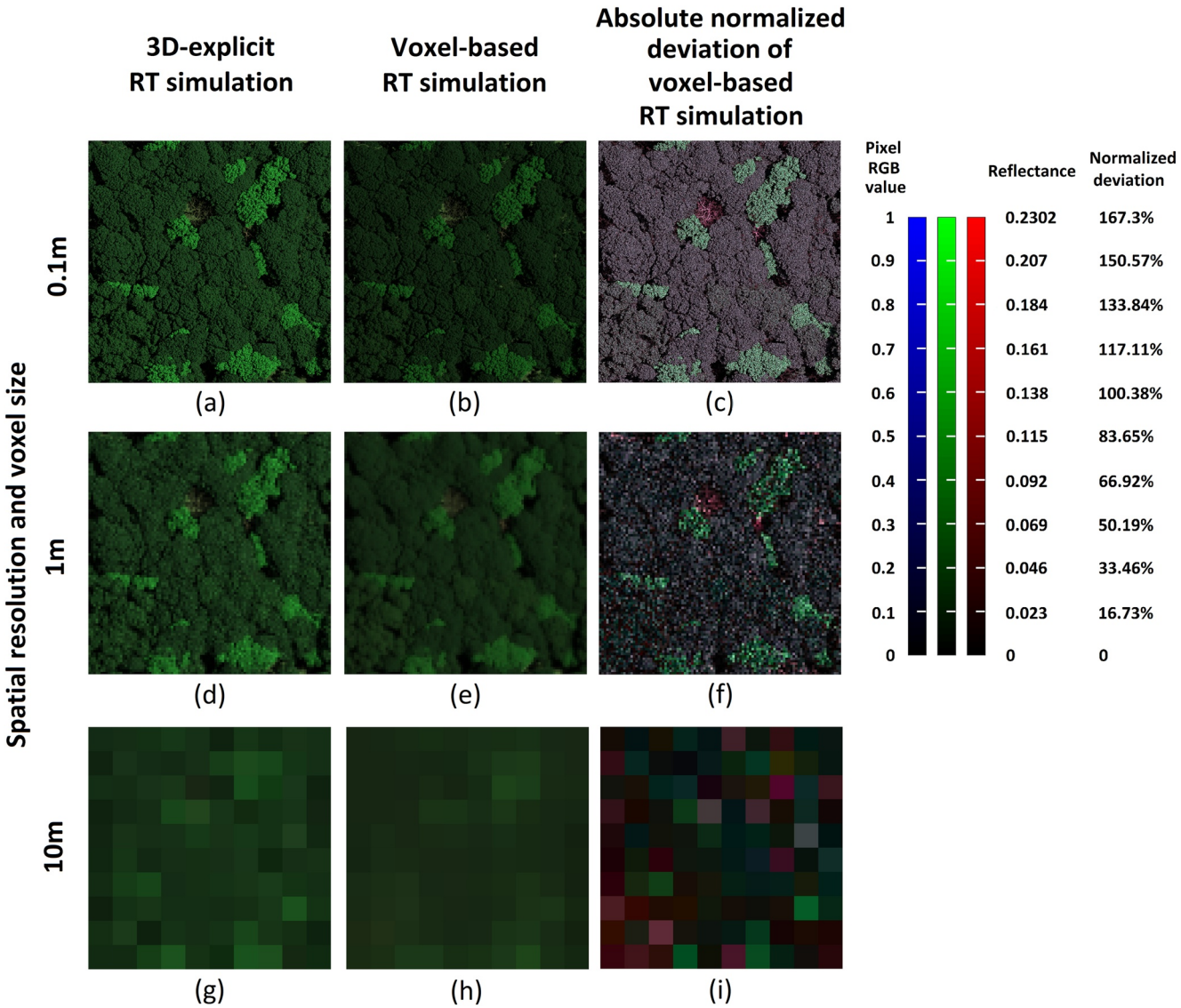


**Figure 5.** Simulated nadir surface reflectance ($\rho_s$) images and deviation images over the 1-ha Wytham Woods plot, with spatial resolutions and voxel sizes 0.1 m (first row), 1 m (second row), and 10 m (third row), respectively. First column: RGB surface reflectance images of 3D-explicit RT simulation. Second column: RGB surface reflectance images of voxel-based RT simulation. Third column: RGB images of absolute normalized deviation of voxel-based RT simulation; results of the 3D-explicit RT simulation with the same simulation settings were used as the benchmark, and the absolute values of normalized surface reflectance deviation in red, green, and blue wavebands were transformed into pixel RGB values. The correspondence between pixel RGB values and reflectance/deviation values is: pixel R, G, and B values 0–1 correspond to reflectance 0–0.2302, and normalized deviation 0 to +167.3%. The images are based on bands 2, 3, and 4 from the MSI instrument on Sentinel-2 (wavelength: 490 ± 32.5, 560 ± 17.5, and 665 ± 15 nm). The simulated sensor was placed at the Bottom of Atmosphere (BOA). For the images of voxel-based RT simulation, the spatial resolutions are equal to the voxel size.

(referred as "wood-ground"). 98.8% of pixels were canopy and canopy gap pixels. Canopy and bare-wood pixels had negative $\rho_s$ deviation values. In contrast, pixels of canopy gap and wood-ground had positive $\rho_s$ deviation values.

In the green waveband, the pixels of English oak canopy, whose leaf had higher reflectance than other tree species (greener in Figure 5), had larger negative $\rho_s$ deviations. This phenomenon also happened in the blue waveband, but it was less obvious. As discussed before, larger leaf reflectance leads to larger normalized $\rho_s$ deviation. In the blue waveband, the leaf reflectance of English oak is also higher than other dominant tree species. But this difference is not as significant as in the green waveband (Table 3). Thus, the normalized deviation in the blue waveband is also smaller compared to the green waveband. In the red waveband, the positive $\rho_s$ deviation of



21698996, 2022, 14, Downloaded from https://agupubs.onlinelibrary.wiley.com/doi/10.1029/2021JD036175 by Portail BibCNRS INSU, Wiley Online Library on [16/03/2023]. See the Terms and Conditions (https://onlinelibrary.wiley.com/terms-and-conditions) on Wiley Online Library for rules of use; OA articles are governed by the applicable Creative Commons License

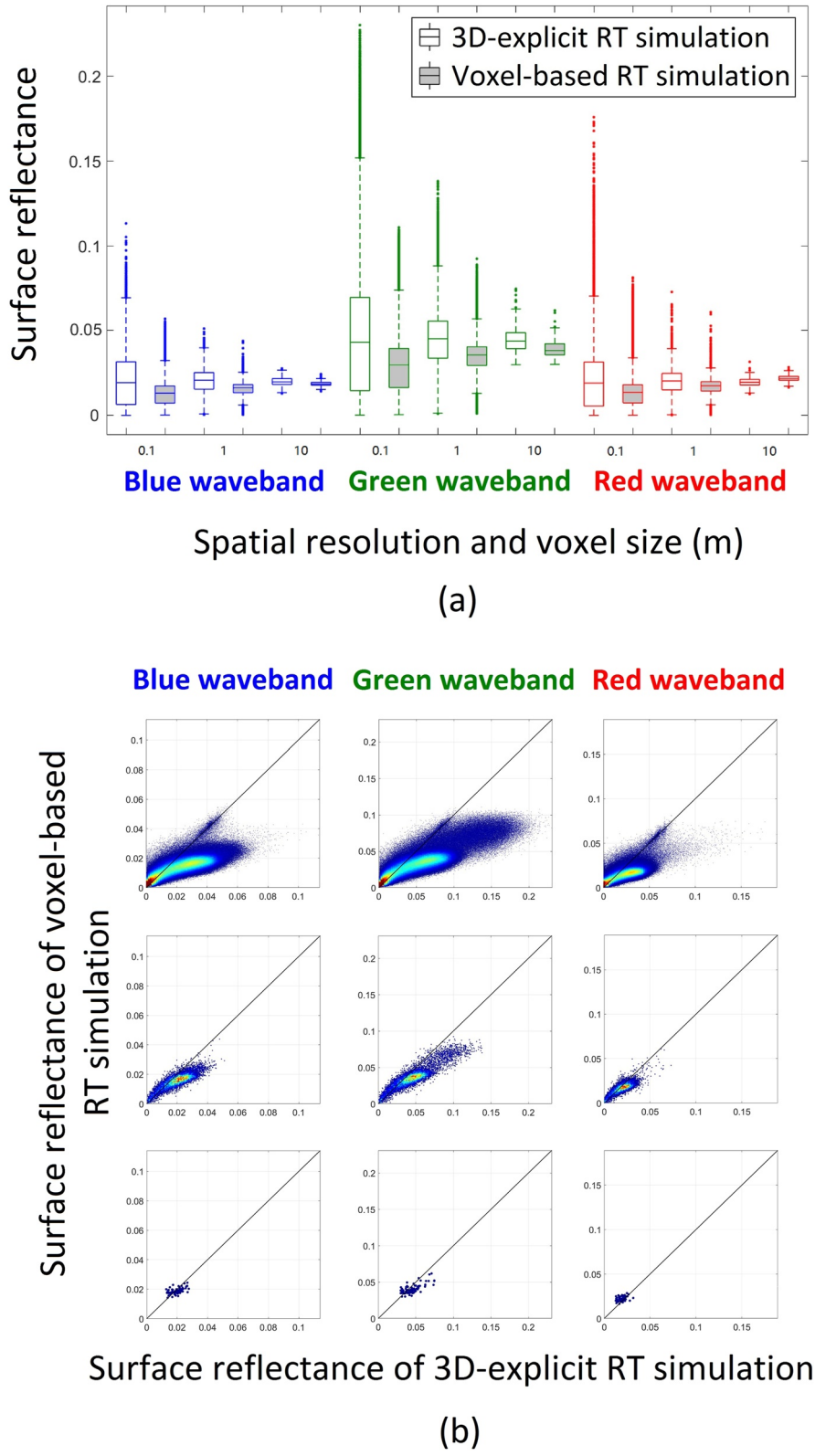


**Figure 6.** Statistics of pixel surface reflectance ($\rho_s$) values of nadir RGB images. (a) boxplot of surface reflectance of each image. Gray boxes are statistics of images of voxel-based RT simulations, under the same simulation conditions as the 3D-explicit images on their left. (b) scatter plots comparing the surface reflectance of different RT simulations pixel by pixel, in spatial resolutions and voxel sizes 0.1 m (first row), 1 m (second row), and 10 m (third row). The three columns show the results of the blue, green, and red waveband, respectively. The solid black line represents the 1:1 line.



21698996, 2022, 14, Downloaded from https://agupubs.onlinelibrary.wiley.com/doi/10.1029/2021JD036175 by Portail BibCNRS INSU, Wiley Online Library on [16/03/2023]. See the Terms and Conditions (https://onlinelibrary.wiley.com/terms-and-conditions) on Wiley Online Library for rules of use; OA articles are governed by the applicable Creative Commons License

**Table 2**
*The Mean Normalized Surface Reflectance Deviations of Nadir Images of Voxel-Based RT Simulation Compared With 3D-Explicit RT Simulation*

| | | Waveband | | | |
|---|---|---|---|---|---|
| | | Blue | Green | Red | NIR |
| Voxel size and spatial resolution (m) | 0.1 | −37.4% | −35.6% | −33% | −22.7% |
| | 1 | −22.2% | −21.6% | −14% | −14.2% |
| | 10 | −5.7% | −12.3% | +12.4% | −27% |

canopy gap and wood-ground pixels became higher. This positive deviation occurred in most pixels in the large voxel size and coarse resolution of 10 m. The negative $\rho_s$ deviation of bare-wood pixels was also larger in the red waveband. For the 0.1 and 1 m voxel size and resolution, the overall $\rho_s$ deviation in the NIR waveband was smaller than RGB wavebands, especially for the wood-ground pixels.

### 3.1.2. Directional Reflectance Deviation Under Multiple View Geometry

The accuracy of voxel-based RT simulations compared to 3D-explicit models varied greatly with view geometry. The accuracy of voxel-based RT simulation did not meet the 5% tolerance criteria under 89% of the hemispheric viewing directions (Figure 8). For the 0.1 m voxel size, the normalized $\rho_d$ deviations were within the 5% tolerance under only two narrow viewing angles for the red waveband: a small region near VZA 80.16° VAA 100.72°; and the hot spot direction, VZA 30° VAA 101°. Deviation values of other viewing directions were negative and exceeded the 5% tolerance limit (Figures 8a–8d).

At the 1 m voxel size, the normalized $\rho_d$ deviations of more viewing directions remained below the 5% tolerance level in red, green, and blue wavebands (white regions in Figures 8e–8g) compared with the 0.1 m voxel size. In the green waveband, these directions were under VZA 50°–70°. In red and blue wavebands, most of these directions were under backwards (defined in Nomenclature) VAA and 50°–70° VZA. The normalized $\rho_d$ deviations under hot spot viewing directions also met the 5% tolerance criteria in the green and blue wavebands. The deviation of only one small region remained below the 5% tolerance criteria in the NIR waveband (viewing direction near VZA 80.16°, VAA 79.54°) (Figure 8h).

For the 10 m voxel size, the normalized $\rho_d$ deviations of much more viewing directions remained below the 5% tolerance level in blue and green wavebands (Figures 8i, 8j). These viewing directions also included the hot spot direction in the green waveband. While in the red waveband, the normalized $\rho_d$ deviations of most viewing directions were positive. The deviations of 9.3% of the viewing directions remained below the 5% tolerance level (Figure 8k). The deviation value of the NIR waveband remained negative and became lower. Deviation of only one small region remained below the 5% tolerance criteria in the NIR waveband (viewing direction near VZA 80.16°, VAA 354.83°) (Figure 8l).

**Table 3**
*The Relationship Between Leaf Reflectance and Normalized $\rho_s$ Deviation for the Other Two Dominant Tree Species, and the Ratio After Divided by That of English Oak*

| Waveband | | | Blue | Green | Red | NIR |
|---|---|---|---|---|---|---|
| Sycamore versus English oak | Leaf reflectance | English oak | 0.058 | 0.153 | 0.049 | 0.428 |
| | | Sycamore | 0.045 | 0.086 | 0.042 | 0.444 |
| | | Ratio (English oak/Sycamore) | 1.29 | 1.78 | 1.17 | 0.96 |
| | Normalized $\rho_s$ deviation | English oak | 67.5% | 83% | 60.1% | 31.2% |
| | | Sycamore | 54.6% | 47.3% | 54.1% | 33.9% |
| | | Ratio | 1.24 | 1.75 | 1.11 | 0.92 |
| Common ash versus English oak | Leaf reflectance | English oak | 0.058 | 0.153 | 0.049 | 0.428 |
| | | Common ash | 0.045 | 0.093 | 0.043 | 0.446 |
| | | Ratio (English oak/common ash) | 1.29 | 1.65 | 1.14 | 0.96 |
| | Normalized $\rho_s$ deviation | English oak | 67.5% | 83% | 60.1% | 31.2% |
| | | Common ash | 50.9% | 48.2% | 51% | 32.9% |
| | | Ratio | 1.33 | 1.72 | 1.18 | 0.95 |

*Note*. Voxel size: 0.1 m.



21698996, 2022, 14, Downloaded from https://agupubs.onlinelibrary.wiley.com/doi/10.1029/2021JD036175 by Portail BibCNRS INSU, Wiley Online Library on [16/03/2023]. See the Terms and Conditions (https://onlinelibrary.wiley.com/terms-and-conditions) on Wiley Online Library for rules of use; OA articles are governed by the applicable Creative Commons License

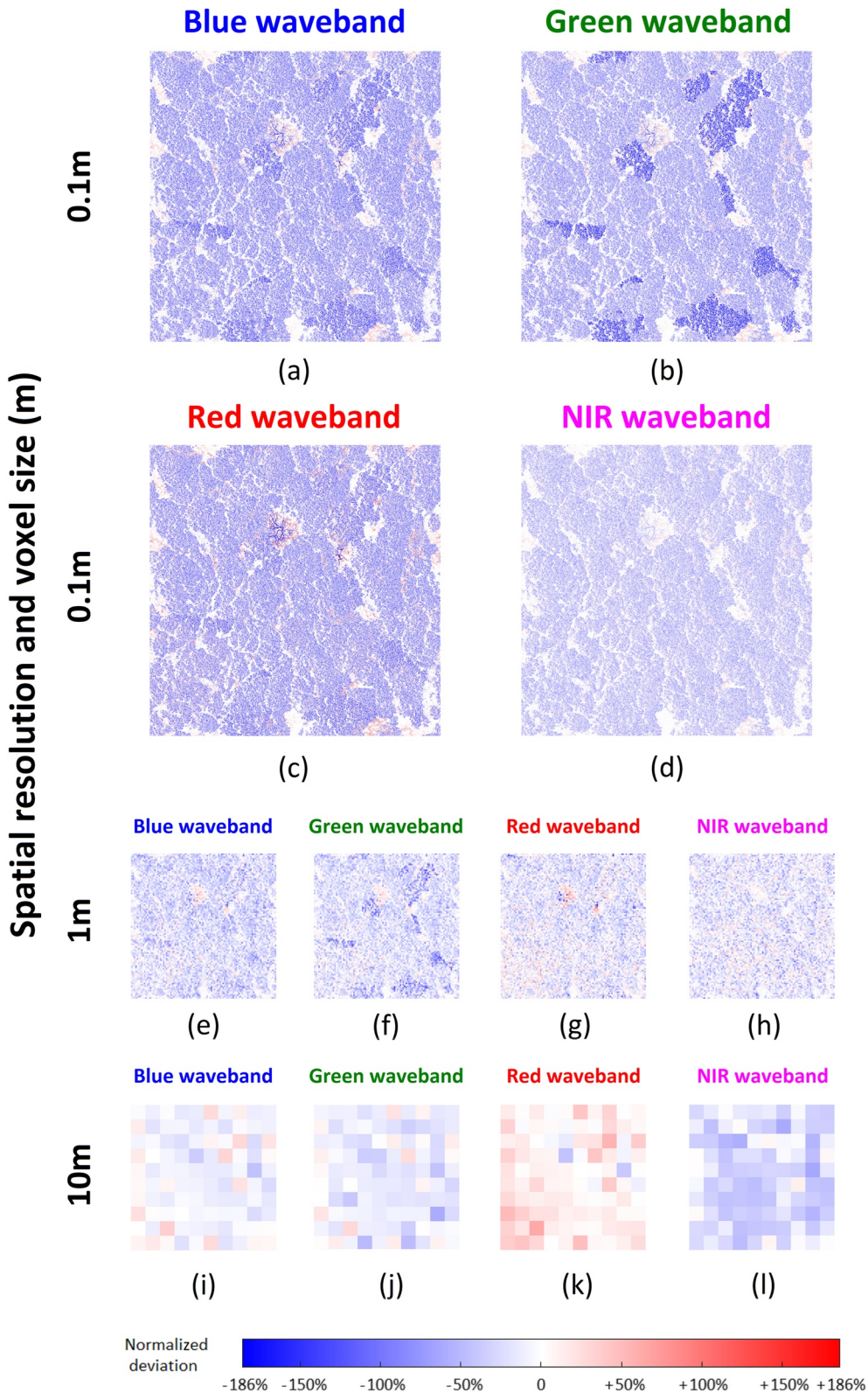


**Figure 7.** Spatial pattern of the normalized surface reflectance ($\rho_s$) deviation for voxel-based RT simulation. Results of the 3D-explicit RT simulation with the same simulation settings were used as the benchmark. (a–d) nadir deviation images with voxel size 0.1 m, in blue, green, red, and NIR wavebands, respectively. (e–h) and (i–l) are nadir deviation images with voxel sizes 1 and 10 m in the above four wavebands. The spatial resolutions of the images are equal to the voxel sizes.



21698996, 2022, 14, Downloaded from https://agupubs.onlinelibrary.wiley.com/doi/10.1029/2021JD036175 by Portail BibCNRS INSU, Wiley Online Library on [16/03/2023]. See the Terms and Conditions (https://onlinelibrary.wiley.com/terms-and-conditions) on Wiley Online Library for rules of use; OA articles are governed by the applicable Creative Commons License

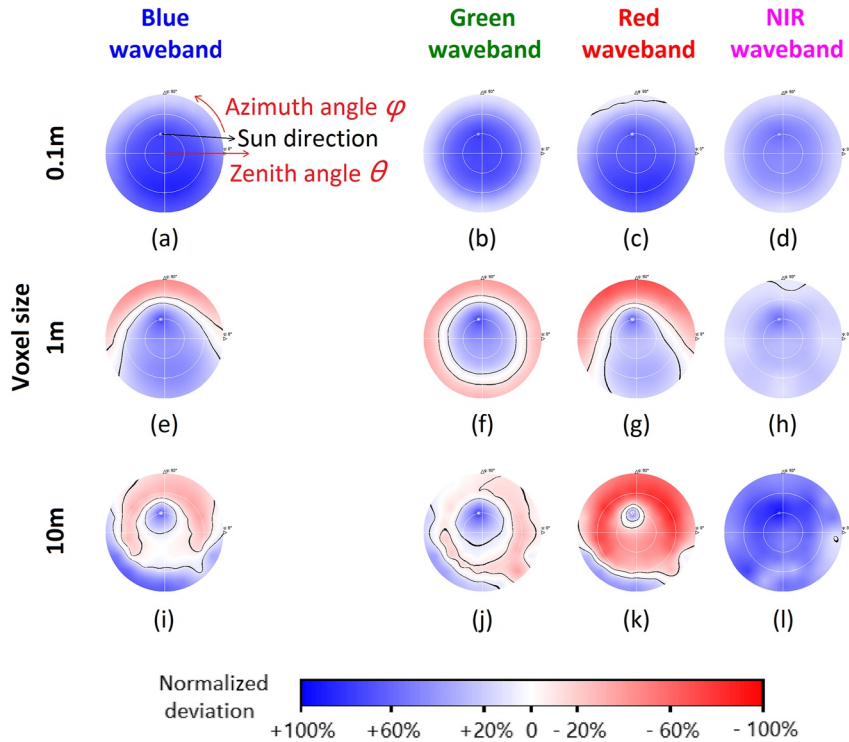


**Figure 8.** The normalized deviation of directional reflectance ($\rho_d$) of voxel-based RT simulation in blue (first column), green (second column), red (third column), and NIR (fourth column) wavebands, with voxel size 0.1 m (top row), 1 m (middle row), and 10 m (bottom row). Results of the 3D-explicit RT simulation with the same simulation settings were used as the benchmark. The view geometry is represented by the polar system. The angular coordinate is viewing azimuth angle (VAA) and the radial coordinate is viewing zenith angle (VZA). The black lines are the contour lines of 5% normalized deviation. The regions within these contour lines are the viewing angles whose normalized $\rho_d$ deviation meets the 5% tolerance criteria.

### 3.1.3. Impact of Voxel Size on Spectral Albedo Deviation

When the voxel size was smaller than 2 m, the accuracy of voxel-based RT simulations decreased as voxel size decreased. Although simulations with very small voxel sizes (0.1–0.5 m) had more accurate outlines in 3D structure, the spectral albedo simulated by them had large negative deviations. Overall, relatively large voxel sizes (1 and 2 m) were most accurate (Figure 9) for the red, green, blue, and NIR wavebands.

In the red and blue wavebands, the normalized deviation value of spectral albedo switched from negative to positive as the voxel size increased. The spectral albedo in red and blue wavebands had minimal deviation with voxel sizes 2 and 10 m, respectively. The minimal deviations were +2% (red waveband) and 0 (blue waveband). In the green and NIR wavebands, the normalized deviation value of spectral albedo was negative for all voxel sizes (0.1–50 m). The normalized deviation value showed an increasing trend up to the maximum value point and then a declining trend. These maximum value points were also the minimal deviation points in the wavebands. The minimal deviation in the green waveband was −3.9%, and the voxel size was 10 m. While in the NIR waveband, the minimal deviation was −13.5%, and the voxel size was 1 m. For each waveband, the normalized spectral albedo deviations under only a few voxel sizes remained below the 5% tolerance criteria.

Voxel sizes similar to the leaf size may lead to deviations in local leaf area values (Béland et al., 2011; Soma et al., 2018), resulting in irregular patterns in simulation results and deviations (Widlowski et al., 2014). This study also tested simulations under this condition. Leaf dimensions in this study ranged from 0.25 to 0.3 m. The results show that when using voxel sizes near leaf size dimension (voxel size: 0.2, 0.25, 0.275, 0.3, and 0.35 m), the normalized deviation of simulated spectral albedo did not have irregular patterns and followed the overall trend (Figure 9).



21698996, 2022, 14, Downloaded from https://agupubs.onlinelibrary.wiley.com/doi/10.1029/2021JD036175 by Portail BibCNRS INSU, Wiley Online Library on [16/03/2023]. See the Terms and Conditions (https://onlinelibrary.wiley.com/terms-and-conditions) on Wiley Online Library for rules of use; OA articles are governed by the applicable Creative Commons License

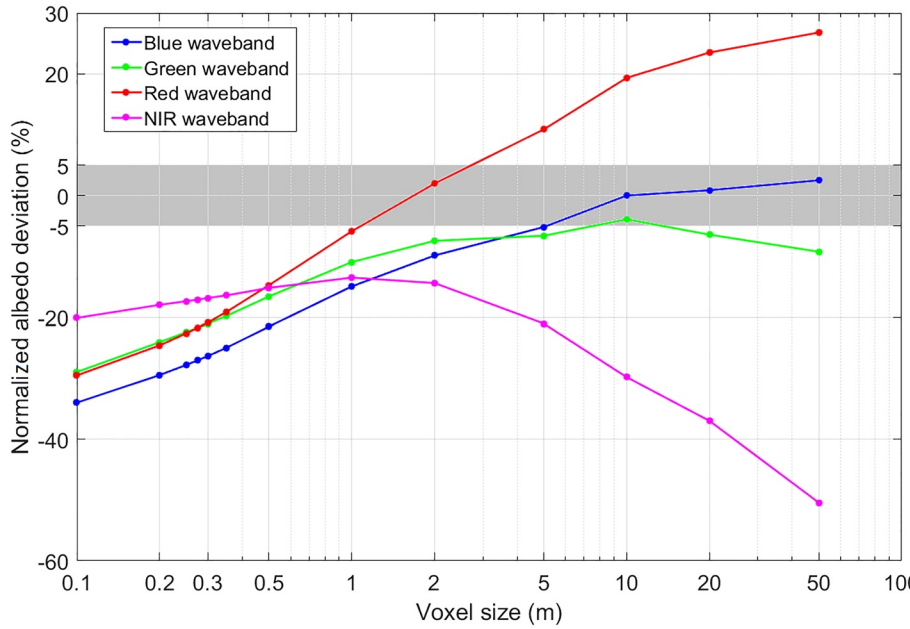


**Figure 9.** Normalized spectral albedo deviation of voxel-based RT simulation under different voxel sizes. Results of the 3D-explicit RT simulation with the same simulation settings were used as the benchmark. The gray area indicates the 5% tolerance region.

### 3.1.4. Spectral Patterns of Spectral Albedo Deviation

The normalized deviation of spectral albedo was negative in most wavebands. The overall trend was that the normalized deviation values slightly increased with increasing wavelength. As the voxel size increased from 0.2 to 1 m and 10 m, the deviation became more sensitive to the wavelength (Figure 10). In certain wavelength regions,

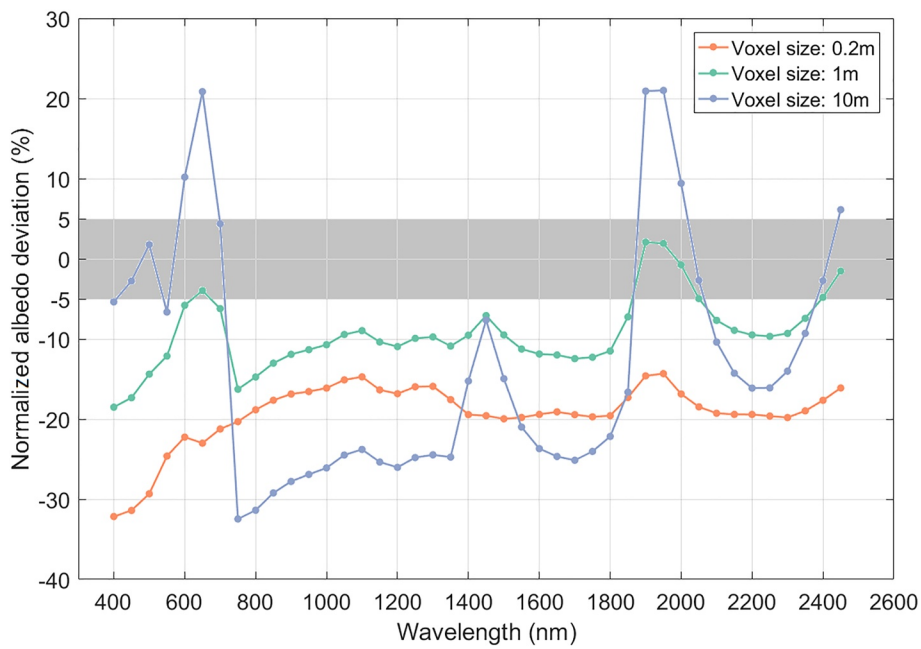


**Figure 10.** The normalized deviation of spectral albedo of voxel-based RT simulation as a function of spectral domain, under voxel size 0.2, 1, and 10 m. The central wavelength of the wavebands is spaced at 50 nm, and the bandwidth of each waveband is 5 nm, which is similar to the hyperspectral remote sensing sensors. Results of the 3D-explicit RT simulation with the same simulation settings were used as the benchmark. The gray area indicates the 5% tolerance region.



21698996, 2022, 14, Downloaded from https://agupubs.onlinelibrary.wiley.com/doi/10.1029/2021JD036175 by Portail BibCNRS INSU, Wiley Online Library on [16/03/2023]. See the Terms and Conditions (https://onlinelibrary.wiley.com/terms-and-conditions) on Wiley Online Library for rules of use; OA articles are governed by the applicable Creative Commons License

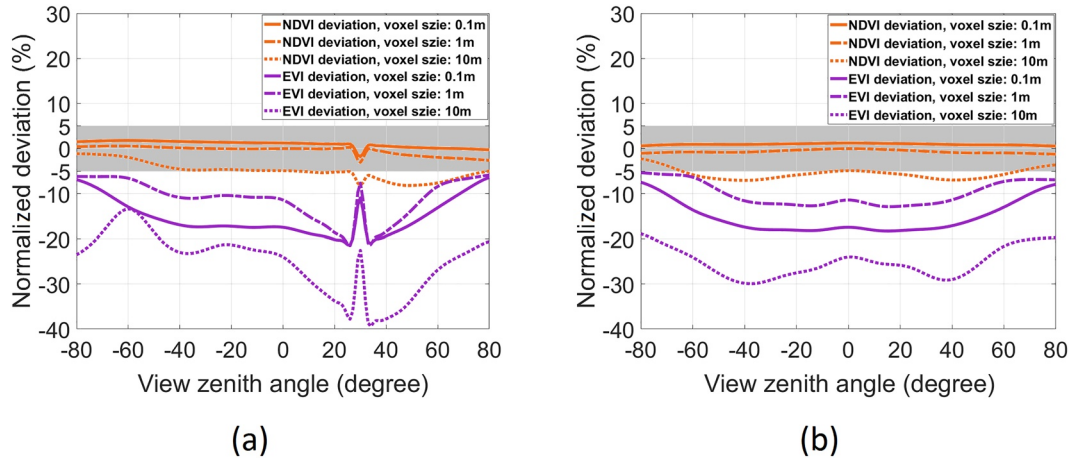


**Figure 11.** The normalized deviation of NDVI and EVI of voxel-based RT simulation, compared with 3D-explicit RT simulation. (a) Deviation on the principal plane; (b) deviation on the orthogonal plane. The gray area indicates the 5% tolerance region.

the normalized deviation value first increased rapidly and then decreased sharply along with the wavelength increase. These regions were: wavelength 550–700 nm, which included red waveband; 1,350–1,600; 1,800–2,150; and 2,300–2,450 nm. As discussed in Section 3.1.1, these peaked values are due to more light reaching the understorey with larger voxel sizes. And the understorey reflected more light than the canopy in these wavebands.

Among the 126 simulation conditions (42 wavebands × three voxel sizes) shown in Figure 10, the normalized deviations of only 12 conditions remained below the 5% tolerance limit. Most of these conditions (10/12) came from the above wavelength regions in which the deviation was more sensitive to the wavelength.

### 3.1.5. Deviation of Vegetation Indices

The simulated NDVI and EVI were analyzed at different voxel sizes (Figure 11). The normalized NDVI deviation value declined from positive to negative as the voxel size increased. For voxel sizes 0.1 and 1 m, the deviation values under all VZAs in principal and orthogonal planes remained below the 5% tolerance criteria. For the 10 m voxel size, only in the forward viewing direction, the NDVI deviation on the principal plane remained below the 5% tolerance level; in the orthogonal plane, the deviation values under large VZAs (larger than 65°) remained below the 5% tolerance limit. In the principal and orthogonal planes, the normalized EVI deviation values were negative and exceeded the 5% tolerance criteria under all voxel sizes (0.1, 1, and 10 m) and VZAs. The normalized EVI deviation value increased first and then declined as the voxel size increased. For the VZAs near the hot spot direction (VZA 30° ± 4°, principal plane), the normalized deviation of NDVI and EVI changed sharply. In the hot spot direction (VZA 30°, principal plane), the normalized NDVI deviation reached the local minimum values, and the normalized EVI deviation reached the local maximum values.

NDVI is nonlinear and saturates in high biomass vegetated areas (Gitelson, 2004; Huete et al., 2002; Ünsalan & Boyer, 2004). The sensitivity of NDVI to leaf area index (LAI) becomes increasingly weak with increasing LAI beyond a threshold value, which is typically between 2 and 3 (Carlson & Ripley, 1997). In contrast, EVI was developed to optimize the vegetation signal with improved sensitivity in high biomass regions (Fang & Liang, 2008). Pinty et al. (2009) investigated the behavior of VIs using red and NIR wavebands through simulations. The LAI of the simulated Wytham Woods forest plot is 3.8 (Calders et al., 2018). NDVI is therefore less sensitive than EVI in this forest plot. The different sensitivity of NDVI and EVI in this forest plot might be the reason for their difference in deviations. As NDVI in this forest plot might be less sensitive to the change of structural representations than EVI, it differs less between voxel-based and 3D-explicit RT simulations.

### 3.1.6. Deviation of the Fraction of Absorbed Photosynthetically Active Radiation

The voxel-based model performs better in the RB simulations compared to TOC simulations. The overall normalized deviation of simulated FAPAR was smaller than that of spectral albedo. For voxel-based RT simulations with different voxel sizes (0.1–50 m), the normalized FAPAR deviation ranged from −1.1% to +6.9%. While for spectral albedo, this range is −50.4% to +26.8%. The normalized deviation of simulated FAPAR increased as



21698996, 2022, 14, Downloaded from https://agupubs.onlinelibrary.wiley.com/doi/10.1029/2021JD036175 by Portail BibCNRS INSU, Wiley Online Library on [16/03/2023]. See the Terms and Conditions (https://onlinelibrary.wiley.com/terms-and-conditions) on Wiley Online Library for rules of use; OA articles are governed by the applicable Creative Commons License

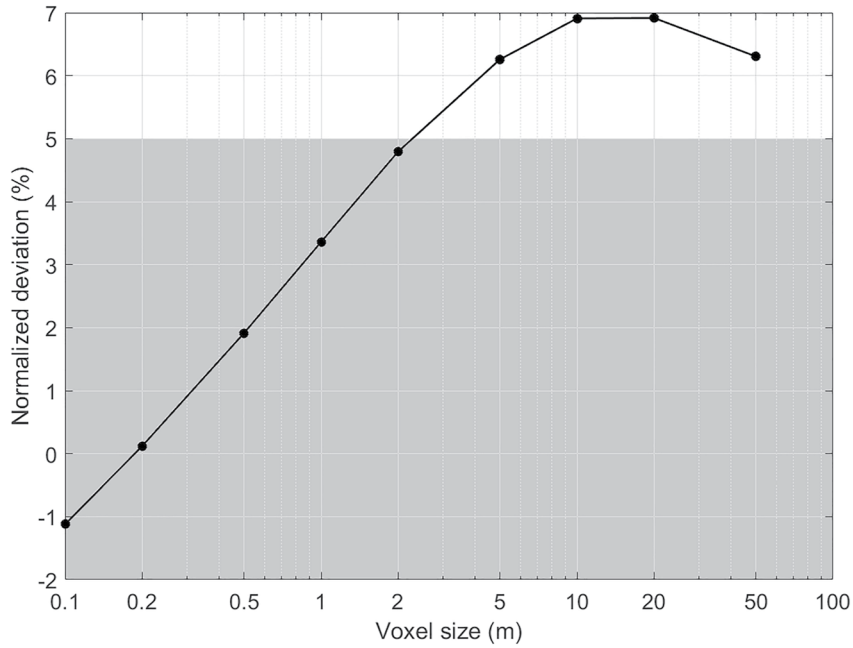


**Figure 12.** The normalized FAPAR deviation of voxel-based RT simulation under different voxel sizes. Results of the 3D-explicit RT simulation with the same simulation settings were used as the benchmark. The gray area indicates the 5% tolerance region.

voxel size increased when voxel size was smaller than 10 m (Figure 12). With voxel size 0.2 m, the voxel-based RT simulation had a very small deviation (+0.12%). And the deviation exceeded the 5% tolerance criteria only when the voxel size was larger than 2 m. The results show that voxel sizes smaller than 2 m are appropriate for the FAPAR simulation in the temperate deciduous forest studied.

### 3.2. Efficiency of 3D-Explicit and Voxel-Based RT Simulations

Voxel-based RT simulations were more computationally efficient than 3D-explicit RT simulations when voxel size was equal to or larger than 1 m (Figure 13). RAM consumption was reduced by 3.8–65.6 times, and time consumption was reduced by 1.1–37.7 times. In general, this improvement increased as the voxel size increased, except for the time consumption at voxel sizes 20–50 m. Voxel-based RT simulation had great efficiency when the voxel size was larger than 5 m. However, these voxel sizes (≥5 m) may be undesirable for RT simulations. Because voxel-based models will lose most of the structural information if they use such large voxel sizes (≥5 m).

For voxel sizes <1 m, the consumption of computational resources of voxel-based RT simulation increased exponentially as the voxel size decreased (Figure 13). RAM and time consumption of voxel-based RT simulation became larger than 3D-explicit RT simulation as the voxel size went below 0.5 m. Voxel-based RT simulation with very small voxels had extensive RAM and time consumption. Voxel-based RT simulation with 0.1 m voxel size required 3254.1 GB RAM and 12385.7 min (approximately 8.6 days) of computational time. These amounts were 7.8 and 15.9 times that of the 3D-explicit RT simulation using the same spatial resolution.

According to the results, voxel sizes of 1–2 m are the optimal selection for the voxel-based model within this forest type. With these voxel sizes, the voxel-based RT simulations are more accurate (Figures 8–11), explained further in Section 3.3.1. And the resource consumption is 1.1–16.5 times less than the 3D-explicit RT simulation (Figure 13).

All RT simulations' RAM and time consumption showed a declining trend up to the minimal value and then an increasing trend as the voxel size increased and the spatial resolution went coarser (Figure 13). DART uses cells (3D cubes) as the basic unit to conduct ray tracking simulation. The cell size is also the voxel size and the spatial resolution of simulated images. DART does not only track rays between cells but also tracks rays within non-empty cells. The scene is first segmented into cells, and then each cell is segmented into $8^3$ subcells. The ray interaction process also happens on subcells:



21698996, 2022, 14, Downloaded from https://agupubs.onlinelibrary.wiley.com/doi/10.1029/2021JD036175 by Portail BibCNRS INSU, Wiley Online Library on [16/03/2023]. See the Terms and Conditions (https://onlinelibrary.wiley.com/terms-and-conditions) on Wiley Online Library for rules of use; OA articles are governed by the applicable Creative Commons License

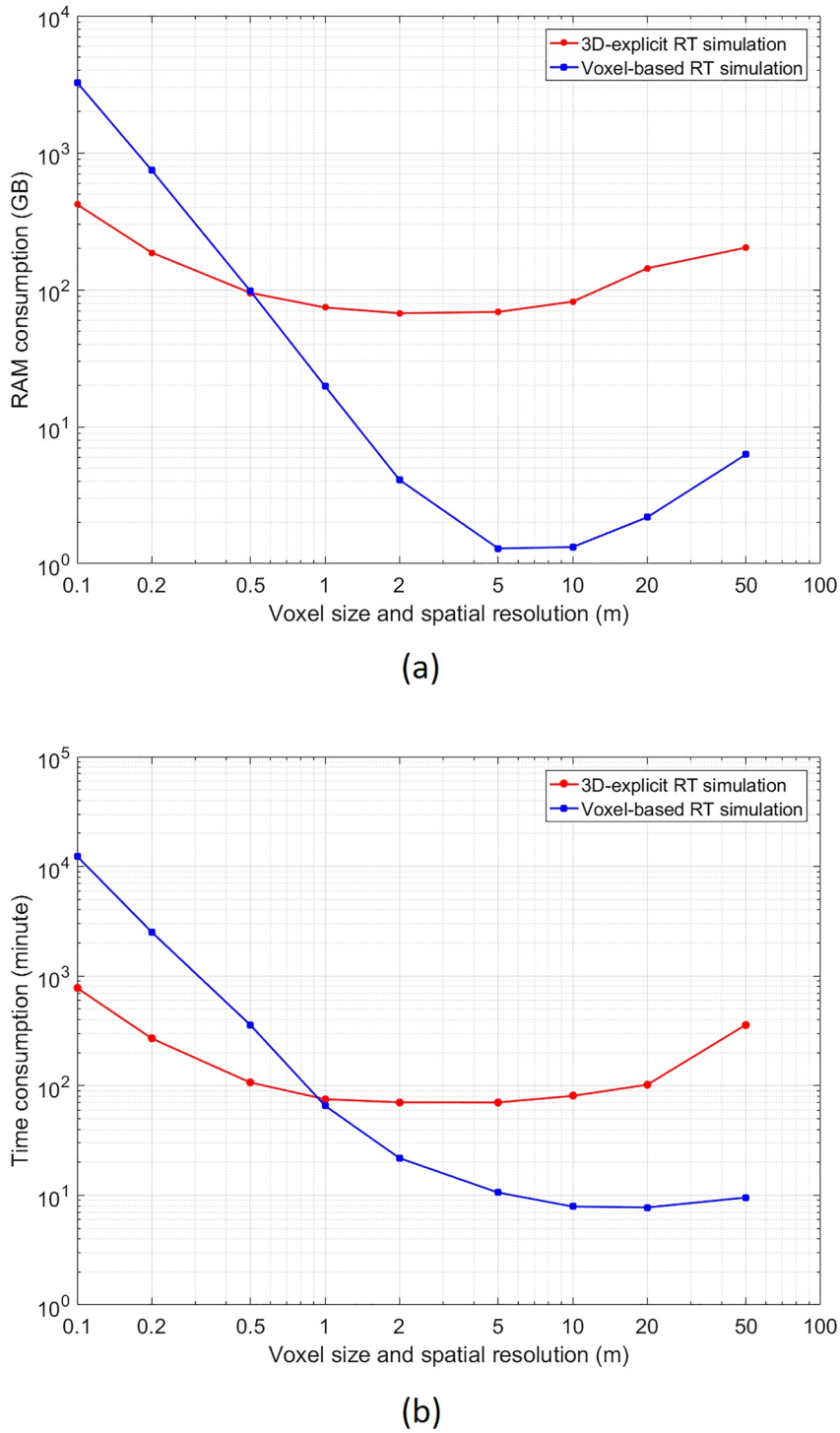


**Figure 13.** Computational resource consumption of 3D-explicit and voxel-based RT simulations: (a) RAM consumption; (b) time consumption. Voxel-based RT simulation with 0.1 m voxel size requires a huge amount of computational resources. Thus it was not conducted in all the 55 wavebands. The consumption of this simulation was deduced from four single waveband simulations. These wavebands were blue, green, red, and NIR wavebands of the MSI instrument on Sentinel-2. The numerical relations in resource consumption between these single waveband simulations and all 55 wavebands simulations were obtained and tested from simulations of other voxel sizes (0.2, 0.25, and 0.5 m).



21698996, 2022, 14, Downloaded from https://agupubs.onlinelibrary.wiley.com/doi/10.1029/2021JD036175 by Portail BibCNRS INSU, Wiley Online Library on [16/03/2023]. See the Terms and Conditions (https://onlinelibrary.wiley.com/terms-and-conditions) on Wiley Online Library for rules of use; OA articles are governed by the applicable Creative Commons License

1. For the 3D-explicit model: in a subcell, the intercepted rays are grouped as a centroid per facet, subcell and angular sector. Then further scattering occurs from each centroid. Rays that exit the cell are grouped as a centroid per subface and angular sector. And further ray tracking occurs from each centroid.
2. For the voxel-based model: like the 3D-explicit model, DART also uses centroids on the voxel-based model for ray tracking. DART uses two centroids per subcell per incident direction and one centroid per subface per exit direction.

As the voxel size increased and the spatial resolution went coarser (i.e., the cell was larger), there were fewer cells in the scene. The tracking of rays between cells was easier and needed fewer computational resources. However, since the cell is larger, each cell and subcell contain more objects. Hence, tracking rays within cells is more complex and needs more computational resources. As the voxel size increased and the spatial resolution went coarser, these two processes had an opposite influence on resource consumption. Therefore, DART simulation did not get the minimal computational resource consumption when using the largest voxel size and the coarsest resolution.

### 3.3. General Discussion

The normalized deviations of voxel-based RT simulations exceeded the tolerance criteria (5%) in 89% viewing directions, 90.5% wavelengths, 65.3% voxel sizes and spatial resolutions, compared with 3D-explicit RT simulations (Figures 8–10, 12). Two major reasons caused the deviations of voxel-based RT simulation: (a) the difference in light interaction. And the simulation deviation (deviation in simulated $\rho_s$, $\rho_d$, spectral albedo, and VIs) caused by it is called the "light interaction deviation," LID (Section 3.3.1); and (b) the structural difference of 3D contour. And the simulation deviation caused by it is called "structural deviation," SD (Section 3.3.2).

#### 3.3.1. Light Interaction Deviation

Light interaction deviation (LID) is the term describing differences in light interaction between the voxel-based and 3D-explicit models due to clumping at scales smaller than the voxel size, and object sizes larger than the scatterer size of turbid medium. When using a voxel size of 0.1 m, the 3D contour of the voxel-based model is very similar to the 3D-explicit model. However, under these circumstances, the normalized $\rho_s$ deviation of voxelized canopies (canopies in Figures 7a–7d) was approximate −53.2% in RGB wavebands (different according to wavebands and tree spectral properties). And the $\rho_s$ deviations of canopy gaps and pure ground pixels were positive. A voxel is a 3D cube filled with an infinite number of infinitely small flat facets at every location, with specified angle distribution, area volume density ($m^2/m^3$), and spectral properties (reflectance, transmittance, and absorptance). The 3D-explicit model comprises solid facets with similar shapes and sizes as real objects (e.g., leaf). The internal structural differences (infinitely small flat facets vs. solid facets) will lead to a light interaction difference and then impact the objects' reflectance, transmittance, and absorptance. For example, for the light reflection of a single object, if the reflectance of the object is 10%, then the solid facet reflects the light only once, and 10% of the light is backscattered; however, in a voxel, there are infinitely small flat facets with different angles and located on every position, the light will be reflected multiple times by these small flat facets, and part of the light could be incorrectly reflected to the forward directions. Thus, less light is reflected by the voxel to the backwards direction. This "direction misleading" in reflection causes the actual reflectance of the voxel to be lower than the spectral properties assigned to the turbid medium inside the voxel.

Light distribution simulations of the one-layer object (Figure 4) confirmed the assumption above. Using the same spectral properties, PAI, and PAD, the voxelized object reflected and absorbed much less light than the 3D-explicit object (−45.6% in RGB wavebands and −6% in NIR waveband) (Table A1) and thus transmitted more light. The results also showed that the LID value was highly related to the spectral properties of the objects inside the voxel. A single-layer object with smaller reflectance had a higher normalized reflectance deviation after the voxelization (Table A1, RGB wavebands vs. NIR waveband).

Due to the above difference in light interaction, less light was reflected and absorbed by the voxelized canopy than by the 3D-explicit canopy. This led to the large negative deviations of canopy $\rho_s$ (Figure 7). At the same time, since less light was reflected or absorbed, more light passed through the voxelized canopy and reached canopy gaps and ground. This part of the light was then reflected by understorey trees or ground, which caused the positive $\rho_s$ deviation of canopy gap and ground pixels (Figure 7). In summary, the overall LID of this voxelized forest scene was negative (Figure 9, Table 2, the case with 0.1 m voxel size).

The structure inside the turbid medium (infinitely small flat facets) is similar to the atmosphere or liquid but not to the solid scene like forests. Compared with the turbid medium, objects in the forest have larger sizes and are not



21698996, 2022, 14, Downloaded from https://agupubs.onlinelibrary.wiley.com/doi/10.1029/2021JD036175 by Portail BibCNRS INSU, Wiley Online Library on [16/03/2023]. See the Terms and Conditions (https://onlinelibrary.wiley.com/terms-and-conditions) on Wiley Online Library for rules of use; OA articles are governed by the applicable Creative Commons License

21698996, 2022, 14, Downloaded from https://agupubs.onlinelibrary.wiley.com/doi/10.1029/2021JD036175 by Portail BibCNRS INSU, Wiley Online Library on [16/03/2023]. See the Terms and Conditions (https://onlinelibrary.wiley.com/terms-and-conditions) on Wiley Online Library for rules of use; OA articles are governed by the applicable Creative Commons License

evenly distributed over the scene. The LID will disappear when reference objects' spatial distribution and size are the same as the turbid medium (infinitely small flat facets on every location). However, this is almost impossible in forest scenes. When using a very small voxel size (e.g., 0.1 m) in the forest scene, only a very limited number of objects or even only part of an object are located inside the voxel. Therefore, the spatial distribution of these objects is simple and very different from the turbid medium case. Thus the LID of the voxel is large. As the voxel size increases (from 0.1 to 2 m), the voxel becomes larger and contains more objects. The spatial distribution of the objects inside the voxel is more complex and becomes closer to the turbid medium case, without reaching it. Thus the LID of this larger voxel is lower than the smaller voxel. This might be a reason why the accuracy of voxel-based RT simulation improved as the voxel size increased from 0.1 to 2 m (Figure 9). Besides RT simulation, the difference in heterogeneity and object size between forest and turbid medium also impacts other voxel-based approaches, for example, leaf area density estimation. Soma et al. (2018) confirmed a strong sensitivity of the leaf area density estimation to discretization arising from vegetation heterogeneity. Béland et al. (2011) suggested that the volume of a voxel side used in LAI estimation should be larger than the size of the scatterers (leaves) if occlusion effects increase.

Widlowski et al. (2014) documented the BRF biases between the deterministic and pseudo-turbid foliage representations of a 30 cm horizontally infinite layer. In their research, the deterministic reference model contained individual leaves of 34.21 $cm^2$, which were evenly distributed with spherical leaf angle distribution. Their reference 3D model was more similar to the turbid medium than our single-layer object. Thus the LID of the corresponding voxel model (pseudo-turbid media) was smaller in their research (−10% to +3%, according to LAI, VZA, and solar zenith angle). However, the radiative transfer functions of voxels are also different in these two studies. This difference could be another reason causing the different LIDs. It should be investigated in future studies.

To reduce the LID, we can use a look-up table method, applying different multiplicative factors to the spectral properties of the turbid medium. Or a new turbid medium could be developed according to the features of forest objects, for example, calibrating the scattering function of the turbid medium by taking into account the heterogeneity and object size inside the voxel.

#### 3.3.2. Structural Deviation

The normalized deviation of spectral albedo of voxel-based RT simulation changed as the voxel size increased (Figure 9). Another reason for this change is the structural difference of contours or object envelopes between the voxel-based and 3D-explicit models. In the Wytham Woods, scene crown shyness is prominent, with small gaps between most crowns (Calders et al., 2018). As the voxel size increased, the total volume of the voxel-based model expanded. Canopy and understorey gaps became smaller and finally disappeared. In this scene, the canopy gaps were filled and disappeared after the voxel size was larger than 2 m, and the understorey gaps disappeared after the voxel size was larger than 5 m. Besides, other structural information of the forest scene also gradually disappeared as the voxel size increased, such as the detailed shape and outline of the trees and forest scene. These apparent 3D structural changes led to a less realistic 3D scene that caused a larger SD.

With a large voxel size (10 m), the detailed shape and outline of the trees and forest scene disappear. The voxel-based scene has a flat outline with such a voxel size, while the outline of the 3D-explicit model is more realistic and discrete. The change in these structures, especially in the digital surface model, impacts the light reflection at the canopy top. This might explain why the normalized $\rho_d$ deviation varied irregularly as the viewing direction changed when using the 10 m voxel size (Figures 8i–8l).

As previously discussed in Sections 3.1.1 and 3.1.4, with the increase of voxel size, the voxelized objects are less clumped and distributed over a larger space from the whole scene perspective. According to the results in Section 3.3.1, compared with the 3D-explicit representation, objects transmit more light if they are distributed more like a turbid medium. Hence, compared with the structure at a smaller voxel size, the structure at a larger voxel size causes more light to reach the understorey. Meanwhile, the understorey reflected considerably more light than the canopy at specific wavelengths (550–700, 1,350–1,600, 1,800–2,150, and 2,300–2,450 nm) (Figure 2c). Combining the above two reasons, more light reached the understorey at the larger voxel size, and the understorey reflected much more light than the canopy in specific wavebands. Therefore, the spectral albedo deviation displayed peaked values and was more sensitive in particular wavelength regions (Figure 10).

As the voxel size increases, both the SD and LID change, resulting in smaller total simulation deviations for some simulation conditions (Figures 9, Figure 10). The accuracy of the voxel-based RT simulations improved as the voxel size increased from 0.1 to 2 m (Figure 9). However, this is an example of the "right" result caused by two

confounding "wrong" reasons. In further studies, the voxel-based models should be optimized to reduce the LID and SD, taking into account the scale dependencies of both the scene and the sensor.

To reduce SD, the edges and gaps of the voxel-based model could be detected and trimmed (Widlowski et al., 2014). The edges and gaps of the voxel-based model could be subdivided to preserve the detail of contours and gaps (Weiser et al., 2021).

## 4. Conclusions

This study quantified the trade-off between 3D detail, RTM accuracy, and computational resources in a temperate deciduous forest stand. We conducted RT modeling of a 1-ha temperate deciduous forest using two highly detailed 3D model representations, namely 3D-explicit and voxel-based models.

Compared with 3D-explicit RT simulations, the normalized deviations of voxel-based RT simulations exceeded the 5% tolerance criteria in 89% viewing directions, 90.5% wavelengths, 65.3% voxel sizes and spatial resolutions. More specifically, with voxel sizes 0.1, 1, and 10 m and in blue, green, red, and near-infrared wavebands, the normalized deviations of simulated directional reflectance exceeded the 5% tolerance limit in 89% viewing directions. With voxel sizes 0.2, 1, and 10 m, the normalized deviations of simulated spectral albedo exceeded the 5% tolerance limit in 90.5% wavelengths. For simulated spectral albedo in blue, green, red, and near-infrared wavebands and FAPAR, the normalized deviations exceeded the 5% tolerance limit in 65.3% voxel sizes and spatial resolutions. For RS calibration and validation activities, accuracy is of utmost importance. The time and resource saving benefits of voxelizing canopy structure are not adequate for the accuracy loss. Thus, the use of a 3D-explicit forest model is preferred. Suppose the voxel-based model is the only choice. In that case, voxel sizes of 1–2 m are the optimal selection for this forest site.

The voxel-based model can be constructed directly from high-quality point cloud data. Using this method, the voxel-based model is easier to build than the 3D-explicit model. Besides, voxel-based RT simulations are much more computationally efficient than 3D-explicit RT simulations in relatively large voxel size and coarse resolution (voxel size and spatial resolution $\geq$1 m). Therefore, the voxel-based model can be used for sites where 3D-explicit modeling is challenging or 3D-explicit RT simulation requires substantial computational resources. For example, large-area tropical forests.

Light interaction deviation and structural deviation were identified as the two major causes of differences between the voxel-based and 3D-explicit RT simulations. Further studies are suggested to tune the voxel-based model for more accurate RT modeling. Some suggested approaches to optimize the model to reduce the deviations are: using multiplicative factors on voxel spectral properties to reduce LID; developing the new turbid medium more appropriate for forest scenes, for example, calibrating the scattering function of the turbid medium by taking into account the heterogeneity and object size inside the voxel; detecting and trimming the edges and gaps of the voxel-based model to reduce SD (e.g., Weiser et al., 2021; Widlowski et al., 2014).

This study provides guidance for choosing the appropriate 3D forest reconstruction approach from TLS data to be used in the RTM of a temperate deciduous forest. In future studies, the performance of RTMs with 3D models from a range of forest types is required to allow for an in-depth understanding of the impact of forest structure representation in RTMs.

## Appendix A

**Table A1**
*The Normalized Deviations of Actual Reflectance, Absorptance, and Transmittance of Single-Layer Voxelized Facet, Compared With 3D-Explicit Facet: (Voxel—Explicit)/Explicit*

| | Reflectance | Absorptance | Transmittance |
|---|---|---|---|
| Blue waveband | −46.3% | −46.4% | +6523.1% |
| Green waveband | −42.7% | −42.7% | +433.3% |
| Red waveband | −47.7% | −47.7% | +5622.4% |
| NIR waveband | −6.0% | −6.0% | +31.4% |



21698996, 2022, 14, Downloaded from https://agupubs.onlinelibrary.wiley.com/doi/10.1029/2021JD036175 by Portail BibCNRS INSU, Wiley Online Library on [16/03/2023]. See the Terms and Conditions (https://onlinelibrary.wiley.com/terms-and-conditions) on Wiley Online Library for rules of use; OA articles are governed by the applicable Creative Commons License

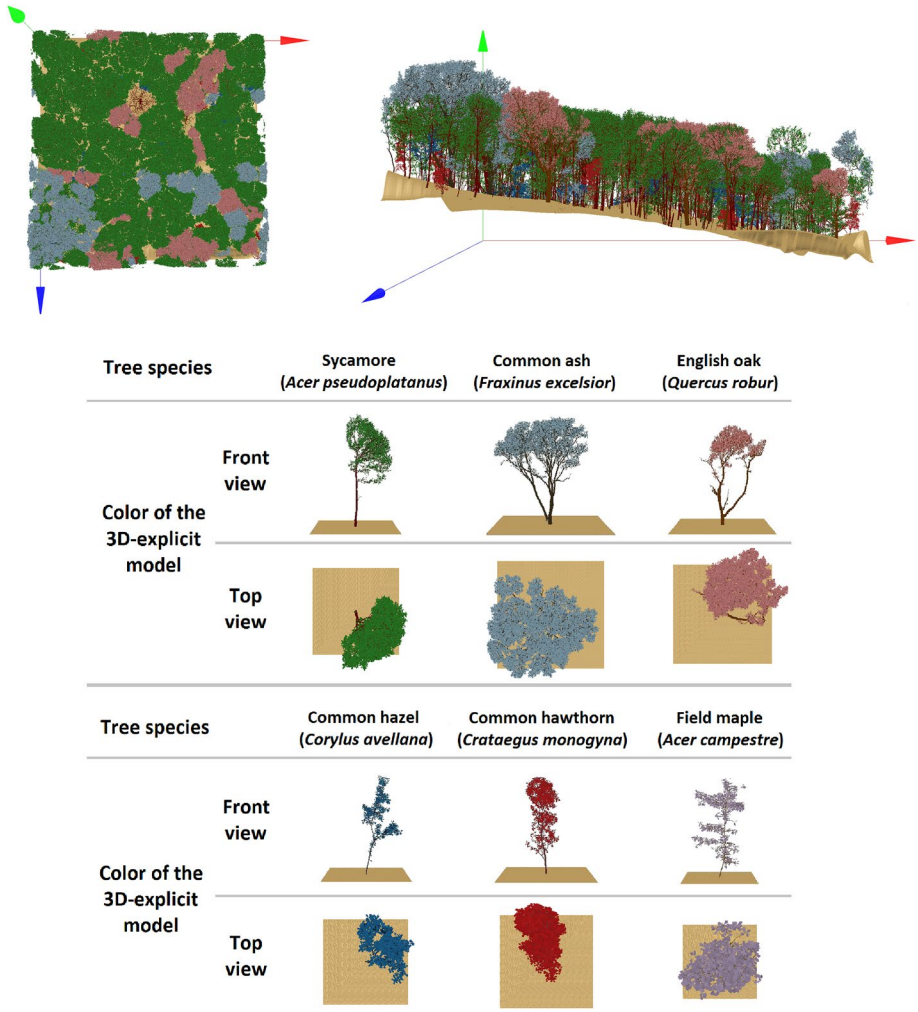


**Figure A1.** The 3D-explicit model of the 1-ha forest plot, in top view (upper left) and front view (upper right). The different colors represent the different tree species present in Wytham Woods.

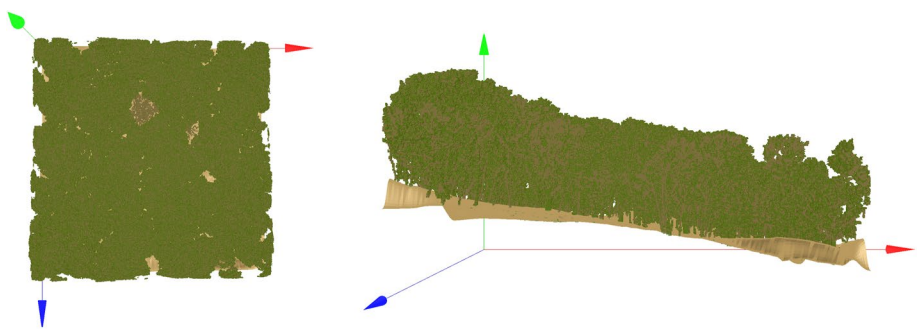

**Figure A2.** Voxel-based model of the 1-ha forest plot, in top view (left) and front view (right). Voxel size: 0.2 m.



21698996, 2022, 14, Downloaded from https://agupubs.onlinelibrary.wiley.com/doi/10.1029/2021JD036175 by Portail BibCNRS INSU, Wiley Online Library on [16/03/2023]. See the Terms and Conditions (https://onlinelibrary.wiley.com/terms-and-conditions) on Wiley Online Library for rules of use; OA articles are governed by the applicable Creative Commons License

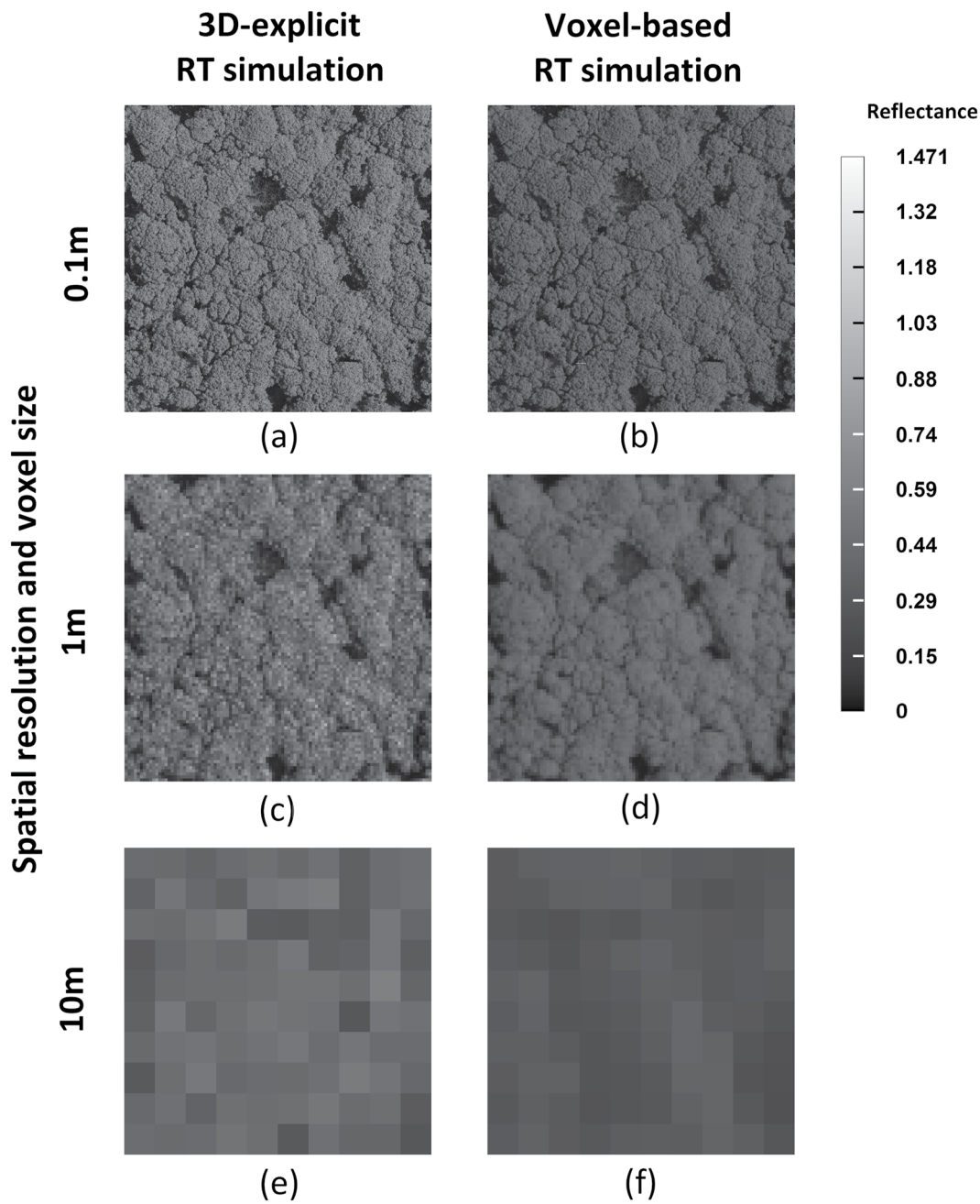


**Figure A3.** Simulated nadir reflectance images over the 1-ha Wytham Woods plot, with spatial resolutions and voxel sizes 0.1 m (first row), 1 m (second row), and 10 m (third row), respectively. First column: NIR surface reflectance images of 3D-explicit RT simulation; second column: NIR surface reflectance images of voxel-based RT simulation.



21698996, 2022, 14, Downloaded from https://agupubs.onlinelibrary.wiley.com/doi/10.1029/2021JD036175 by Portail BibCNRS INSU, Wiley Online Library on [16/03/2023]. See the Terms and Conditions (https://onlinelibrary.wiley.com/terms-and-conditions) on Wiley Online Library for rules of use; OA articles are governed by the applicable Creative Commons License

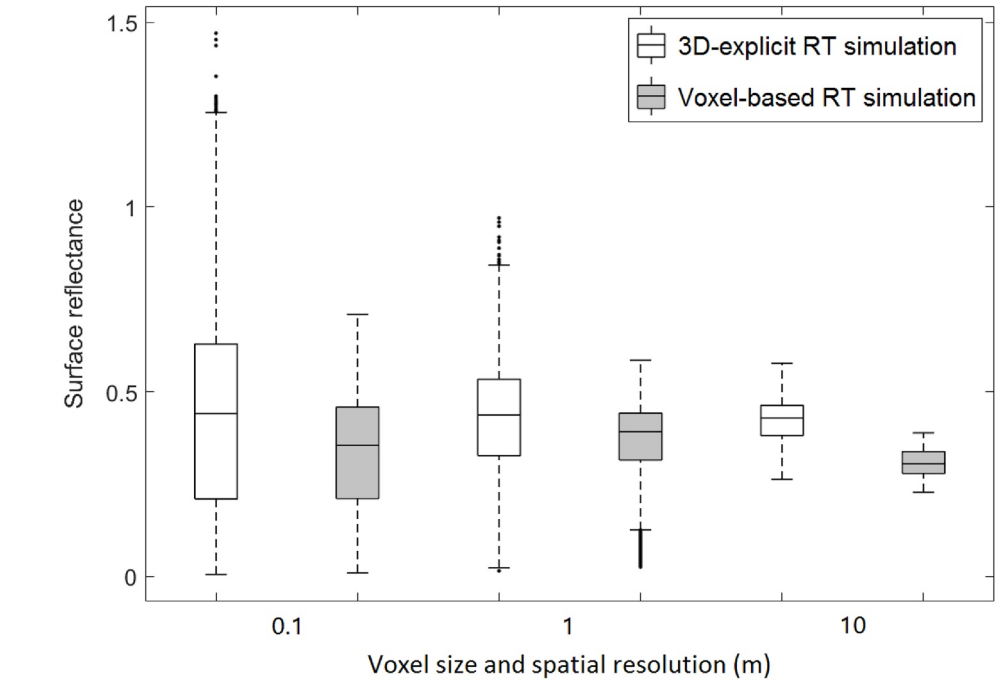


(a)

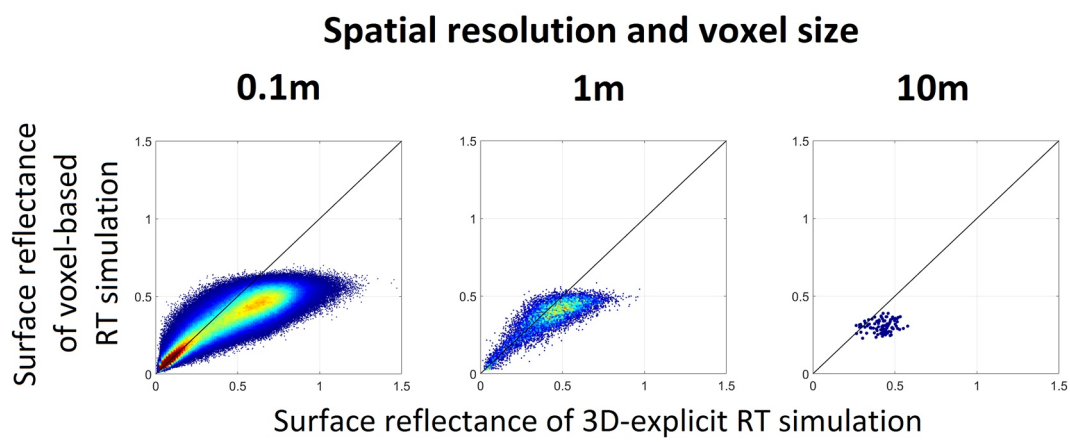


(b)

**Figure A4.** Statistics of pixel surface reflectance (ρs) values of nadir NIR images. (a) Boxplot of surface reflectance of each image. Gray boxes are statistics of images of voxel-based RT simulations, under the same simulation conditions as the 3D-explicit images on their left. (b) Scatter plots that compare the surface reflectance of different RT simulations pixel by pixel, in spatial resolutions and voxel sizes 0.1 m (left), 1 m (middle), and 10 m (right). The solid black line represents the 1:1 line.

## Nomenclature

BOA: Bottom of Atmosphere.
Backwards viewing direction: The viewing direction on the same side of the local vertical as the sun.
Forward viewing direction: The viewing direction on the opposite side of the local vertical as the sun.
Hot spot: Configuration such that the sun is in the back of the sensor.
Nadir image: Image acquired at the vertical (i.e., VZA is 0°).



21698996, 2022, 14, Downloaded from https://agupubs.onlinelibrary.wiley.com/doi/10.1029/2021JD036175 by Portail BibCNRS INSU, Wiley Online Library on [16/03/2023]. See the Terms and Conditions (https://onlinelibrary.wiley.com/terms-and-conditions) on Wiley Online Library for rules of use; OA articles are governed by the applicable Creative Commons License

Orthogonal plane: The vertical plane whose viewing azimuth angle differs by ±90 degrees from that of the principal plane.
Principal plane: The vertical plane which has the same viewing azimuth angle as the sun direction.
RB: Radiative budget.
RB simulation: RB simulation is an RT simulation that outputs the light interaction (reflection, absorption, and transmission) and light distribution within the scene.
RS: Remote sensing.
RT: Radiative transfer.
Spectral Albedo: The ratio between the reflected energy and the incident energy over the scene, on a specific waveband.
TOC: Top of canopy.
TOC simulation: TOC simulation is an RT simulation that outputs the RS data observed at the top of the canopy (e.g., reflectance, albedo, and VIs).
VIs: Vegetation indices.
Voxel-based RT simulation: Radiative transfer simulation with voxel-based forest model as structural input.
Voxel size: The side length of the voxel.
VZA: Viewing zenith angle.
VAA: Viewing azimuth angle.
$\rho_s$: Surface reflectance. The fraction of incoming solar radiation that is reflected from the scene's surface for specific incidents or viewing cases.
$\rho_d$: Directional reflectance. The mean surface reflectance of the whole scene in a specific viewing direction.
3D-explicit RT simulation: Radiative transfer simulation with 3D-explicit forest model as structural input.

## Data Availability Statement

The data set used as 3D structural model for radiative transfer modeling in the study are available at OSF repository via https://doi.org/10.17605/OSF.IO/KYNDW (Liu et al., 2022), this data set is available for download for research and educational purposes.

**Acknowledgments**
CL was funded by the China Scholarship Council (CSC) (No. 201906600031). KC was funded by the European Union's Horizon 2020 research and innovation programme under the Marie Sklodowska-Curie grant agreement No 835398. FM was funded by the FWO as a junior postdoc (fellowship 1214720N). MD acknowledges funding from NERC National Centre for Earth Observation (NCEO). NO's contribution to this project has received funding from the EMPIR programme co-financed by the Participating States and from the European Union's Horizon 2020 research and innovation programme. WW is supported by an Australian Research Council DECRA Fellowship (DE190101182). The computational resources and services used in this work were provided by the VSC (Flemish Supercomputer Center), funded by the Research Foundation—Flanders (FWO) and the Flemish Government—department EWI.

## References

Åkerblom, M., & Kaitaniemi, P. (2021). Terrestrial laser scanning: A new standard of forest measuring and modelling? *Annals of Botany*, *128*(6), 653–662. https://doi.org/10.1093/aob/mcab111
Åkerblom, M., Raumonen, P., Casella, E., Disney, M. I., Danson, F. M., Gaulton, R., et al. (2018). Non-intersecting leaf insertion algorithm for tree structure models. *Interface Focus*, *8*(2), 20170045. https://doi.org/10.1098/rsfs.2017.0045
Bailey, B. N., & Mahaffee, W. F. (2017). Rapid measurement of the three-dimensional distribution of leaf orientation and the leaf angle probability density function using terrestrial LiDAR scanning. *Remote Sensing of Environment*, *194*, 63–76. https://doi.org/10.1016/j.rse.2017.03.011
Béland, M., & Kobayashi, H. (2021). Mapping forest leaf area density from multiview terrestrial lidar. *Methods in Ecology and Evolution*, *12*(4), 619–633. https://doi.org/10.1111/2041-210X.13550
Béland, M., Widlowski, J. L., Fournier, R. A., Côté, J. F., & Verstraete, M. M. (2011). Estimating leaf area distribution in savanna trees from terrestrial LiDAR measurements. *Agricultural and Forest Meteorology*, *151*(9), 1252–1266. https://doi.org/10.1016/j.agrformet.2011.05.004
Bojinski, S., Verstraete, M., Peterson, T. C., Richter, C., Simmons, A., & Zemp, M. (2014). The concept of essential climate variables in support of climate research, applications, and policy. *Bulletin of the American Meteorological Society*, *95*(9), 1431–1443. https://doi.org/10.1175/BAMS-D-13-00047.1
Bruegge, C. J., Chrien, N. L., Ando, R. R., Diner, D. J., Abdou, W. A., Helmlinger, M. C., et al. (2002). Early validation of the multi-angle imaging SpectroRadiometer (MISR) radiometric scale. *IEEE Transactions on Geoscience and Remote Sensing*, *40*(7), 1477–1492. https://doi.org/10.1109/TGRS.2002.801583
Calders, K., Adams, J., Armston, J., Bartholomeus, H., Bauwens, S., Bentley, L. P., et al. (2020). Terrestrial laser scanning in forest ecology: Expanding the horizon. *Remote Sensing of Environment*, *251*, 112102. https://doi.org/10.1016/j.rse.2020.112102
Calders, K., Burt, A., Origo, N., Disney, M., Nightingale, J., Raumonen, P., & Lewis, P. (2016). Large-area virtual forests from terrestrial laser scanning data. In *International geoscience and remote sensing symposium* (Vol. 2016). (IGARSS). https://doi.org/10.1109/IGARSS.2016.7729452
Calders, K., Lewis, P., Disney, M., Verbesselt, J., & Herold, M. (2013). Investigating assumptions of crown archetypes for modelling LiDAR returns. *Remote Sensing of Environment*, *134*, 39–49. https://doi.org/10.1016/j.rse.2013.02.018
Calders, K., Newnham, G., Burt, A., Murphy, S., Raumonen, P., Herold, M., et al. (2015). Nondestructive estimates of above-ground biomass using terrestrial laser scanning. *Methods in Ecology and Evolution*, *6*(2), 198–208. https://doi.org/10.1111/2041-210X.12301
Calders, K., Origo, N., Burt, A., Disney, M., Nightingale, J., Raumonen, P., et al. (2018). Realistic forest stand reconstruction from terrestrial LiDAR for radiative transfer modelling. *Remote Sensing*, *10*(6), 933. https://doi.org/10.3390/rs10060933
Carlson, T. N., & Ripley, D. A. (1997). On the relation between NDVI, fractional vegetation cover, and leaf area index. *Remote Sensing of Environment*, *62*(3), 241–252. https://doi.org/10.1016/S0034-4257(97)00104-1
Cescatti, A. (1997). Modelling the radiative transfer in discontinuous canopies of asymmetric crowns. I. Model structure and algorithms. *Ecological Modelling*, *101*(2–3), 263–274. https://doi.org/10.1016/S0304-3800(97)00050-1



21698996, 2022, 14, Downloaded from https://agupubs.onlinelibrary.wiley.com/doi/10.1029/2021JD036175 by Portail BibCNRS INSU, Wiley Online Library on [16/03/2023]. See the Terms and Conditions (https://onlinelibrary.wiley.com/terms-and-conditions) on Wiley Online Library for rules of use; OA articles are governed by the applicable Creative Commons License

Cifuentes, R., Van der Zande, D., Salas-Eljatib, C., Farifteh, J., & Coppin, P. (2018). A simulation study using terrestrial LiDAR point cloud data to quantify spectral variability of a broad-leaved forest canopy. *Sensors (Switzerland)*, *18*(10), 3357. https://doi.org/10.3390/s18103357

Côté, J. F., Widlowski, J. L., Fournier, R. A., & Verstraete, M. M. (2009). The structural and radiative consistency of three-dimensional tree reconstructions from terrestrial lidar. *Remote Sensing of Environment*, *113*(5), 1067–1081. https://doi.org/10.1016/j.rse.2009.01.017

Disney, M. (2019). Terrestrial LiDAR: A three-dimensional revolution in how we look at trees. *New Phytologist*, *222*(4), 1736–1741. https://doi.org/10.1111/nph.15517

Disney, M. I., Kalogirou, V., Lewis, P., Prieto-Blanco, A., Hancock, S., & Pfeifer, M. (2010). Simulating the impact of discrete-return lidar system and survey characteristics over young conifer and broadleaf forests. *Remote Sensing of Environment*, *114*(7), 1546–1560. https://doi.org/10.1016/j.rse.2010.02.009

Disney, M. I., Lewis, P., Gomez-Dans, J., Roy, D., Wooster, M. J., & Lajas, D. (2011). 3D radiative transfer modelling of fire impacts on a two-layer savanna system. *Remote Sensing of Environment*, *115*(8), 1866–1881. https://doi.org/10.1016/j.rse.2011.03.010

Disney, M. I., Lewis, P. E., Bouvet, M., Prieto-Blanco, A., & Hancock, S. (2009). Quantifying surface reflectivity for spaceborne lidar via two independent methods. *IEEE Transactions on Geoscience and Remote Sensing*, *47*(9), 3262–3271. https://doi.org/10.1109/TGRS.2009.2019268

Ebengo, D. M., De Boissieu, F., Vincent, G., Weber, C., & Féret, J. B. (2021). Simulating imaging spectroscopy in tropical forest with 3d radiative transfer modeling. *Remote Sensing*, *13*(11), 2120. https://doi.org/10.3390/rs13112120

Fang, H., & Liang, S. (2008). Leaf area index models. In *Encyclopedia of ecology, five-volume set* (pp. 2139–2148). Academic Press. https://doi.org/10.1016/B978-008045405-4.00190-7

Gastellu-Etchegorry, J. P. (2008). 3D modeling of satellite spectral images, radiation budget and energy budget of urban landscapes. *Meteorology and Atmospheric Physics*, *102*(3–4), 187–207. https://doi.org/10.1007/s00703-008-0344-1

Gastellu-Etchegorry, J. P. (2021). DART user's manual (5.7.9). Retrieved from https://dart.omp.eu/Public/documentation/contenu/documentation/DART_User_Manual.pdf

Gastellu-Etchegorry, J. P., Demarez, V., Pinel, V., & Zagolski, F. (1996). Modeling radiative transfer in heterogeneous 3-D vegetation canopies. *Remote Sensing of Environment*, *58*(2), 131–156. https://doi.org/10.1016/0034-4257(95)00253-7

Gastellu-Etchegorry, J. P., Grau, E., & Lauret, N. (2012). DART: A 3D model for remote sensing images and radiative budget of Earth surfaces. In *Modeling and simulation in engineering*. https://doi.org/10.5772/31315

Gastellu-Etchegorry, J. P., Martin, E., & Gascon, F. (2004). DART: A 3D model for simulating satellite images and studying surface radiation budget. *International Journal of Remote Sensing*, *25*(1), 73–96. https://doi.org/10.1080/0143116031000115166

Gitelson, A. A. (2004). Wide dynamic range vegetation index for remote quantification of biophysical characteristics of vegetation. *Journal of Plant Physiology*, *161*(2), 165–173. https://doi.org/10.1078/0176-1617-01176

Gobron, N., Pinty, B., Verstraete, M. M., & Govaerts, Y. (1997). A semidiscrete model for the scattering of light by vegetation. *Journal of Geophysical Research Atmospheres*, *102*(8), 9431–9446. https://doi.org/10.1029/96jd04013

Hackenberg, J., Spiecker, H., Calders, K., Disney, M., & Raumonen, P. (2015). SimpleTree - an efficient open source tool to build tree models from TLS clouds. *Forests*, *6*(11), 4245–4294. https://doi.org/10.3390/f6114245

Hosoi, F., & Omasa, K. (2006). Voxel-based 3-D modeling of individual trees for estimating leaf area density using high-resolution portable scanning lidar. *IEEE Transactions on Geoscience and Remote Sensing*, *44*(12), 3610–3618. https://doi.org/10.1109/TGRS.2006.881743

Hosoi, F., & Omasa, K. (2015). Estimating leaf inclination angle distribution of broad-leaved trees in each part of the canopies by a high-resolution portable scanning lidar. *Journal of Agricultural Meteorology*, *71*(2), 136–141. https://doi.org/10.2480/agrmet.D-14-00049

Huete, A., Didan, K., Miura, T., Rodriguez, E. P., Gao, X., & Ferreira, L. G. (2002). Overview of the radiometric and biophysical performance of the MODIS vegetation indices. *Remote Sensing of Environment*, *83*(1–2), 195–213. https://doi.org/10.1016/S0034-4257(02)00096-2

Jacquemoud, S., Verhoef, W., Baret, F., Bacour, C., Zarco-Tejada, P. J., Asner, G. P., et al. (2009). PROSPECT + SAIL models: A review of use for vegetation characterization. *Remote Sensing of Environment*, *113*(Suppl. 1), S56–S66. https://doi.org/10.1016/j.rse.2008.01.026

Janoutová, R., Homolová, L., Malenovskỳ, Z., Hanuš, J., Lauret, N., & Gastellu-Etchegorry, J. P. (2019). Influence of 3D spruce tree representation on accuracy of airborne and satellite forest reflectance simulated in DART. *Forests*, *10*(3), 292. https://doi.org/10.3390/f10030292

Janoutová, R., Homolová, L., Novotný, J., Navrátilová, B., Pikl, M., & Malenovský, Z. (2021). Detailed reconstruction of trees from terrestrial laser scans for remote sensing and radiative transfer modelling applications. *in Silico Plants*, *3*(2), diab026. https://doi.org/10.1093/insilicoplants/diab026

Juchheim, J., Annighöfer, P., Ammer, C., Calders, K., Raumonen, P., & Seidel, D. (2017). How management intensity and neighborhood composition affect the structure of beech (*Fagus sylvatica* L.) trees. *Trees - Structure and Function*, *31*(5), 1723–1735. https://doi.org/10.1007/s00468-017-1581-z

Kallel, A. (2010). Vegetation radiative transfer modeling based on virtual flux decomposition. *Journal of Quantitative Spectroscopy and Radiative Transfer*, *111*(10), 1389–1405. https://doi.org/10.1016/j.jqsrt.2010.02.010

Kirby, K. J., Bazely, D. R., Goldberg, E. A., Hall, J. E., Isted, R., Perry, S. C., & Thomas, R. C. (2014). Changes in the tree and shrub layer of Wytham Woods (Southern England) 1974-2012: Local and national trends compared. *Forestry*, *87*(5), 663–673. https://doi.org/10.1093/forestry/cpu026

Kneubuhler, M., Schaepman, M., Thome, K., Baret, F., & Muller, A. (2002). Calibration and validation of Envisat MERIS Part 1: Vicarious calibration at Rail Road Valley Playa (NV). *Proceedings of MERIS Level 2 Validation Workshop, ESRIN, Frascati, Italy, December*, *9*(1), 13.

Kobayashi, H., & Iwabuchi, H. (2008). A coupled 1-D atmosphere and 3-D canopy radiative transfer model for canopy reflectance, light environment, and photosynthesis simulation in a heterogeneous landscape. *Remote Sensing of Environment*, *112*(1), 173–185. https://doi.org/10.1016/j.rse.2007.04.010

Kükenbrink, D., Schneider, F. D., Schmid, B., Gastellu-Etchegorry, J. P., Schaepman, M. E., & Morsdorf, F. (2021). Modelling of three-dimensional, diurnal light extinction in two contrasting forests. *Agricultural and Forest Meteorology*, *296*, 108230. https://doi.org/10.1016/j.agrformet.2020.108230

Li, W., Guo, Q., Tao, S., & Su, Y. (2018). VBRT: A novel voxel-based radiative transfer model for heterogeneous three-dimensional forest scenes. *Remote Sensing of Environment*, *206*, 318–335. https://doi.org/10.1016/j.rse.2017.12.043

Liang, S., & Wang, J. (2020). Chapter 3 - compositing, smoothing, and gap-filling techniques. In S. Liang & J. Wang (Eds.), *Advanced remote sensing* (2nd ed.) (pp. 107–130). Academic Press. https://doi.org/10.1016/B978-0-12-815826-5.00003-9

Liang, X., Kankare, V., Hyyppä, J., Wang, Y., Kukko, A., Haggrén, H., et al. (2016). Terrestrial laser scanning in forest inventories. *ISPRS Journal of Photogrammetry and Remote Sensing*, *115*, 63–77. https://doi.org/10.1016/j.isprsjprs.2016.01.006

Lintermann, B., & Deussen, O. (1999). Interactive modeling of plants. *IEEE Computer Graphics and Applications*, *19*(1), 56–65. https://doi.org/10.1109/38.736469

Liu, C., Calders, K., Origo, N., Disney, M., & Nightingale, J. (2022). *3D-explicit and voxel-based forest models of Wytham Woods, DART version* [Dataset]. OSF. https://doi.org/10.17605/OSF.IO/KYNDW



21698996, 2022, 14, Downloaded from https://agupubs.onlinelibrary.wiley.com/doi/10.1029/2021JD036175 by Portail BibCNRS INSU, Wiley Online Library on [16/03/2023]. See the Terms and Conditions (https://onlinelibrary.wiley.com/terms-and-conditions) on Wiley Online Library for rules of use; OA articles are governed by the applicable Creative Commons License

Liu, R., Ren, H., Liu, S., Liu, Q., Yan, B., & Gan, F. (2018). Generalized FPAR estimation methods from various satellite sensors and validation. *Agricultural and Forest Meteorology*, *260*, 261–272. https://doi.org/10.1016/j.agrformet.2018.05.024

Ni, W., Li, X., Woodcock, C. E., Caetano, M. R., & Strahler, A. H. (1999). An analytical hybrid GORT model for bidirectional reflectance over discontinuous plant canopies. *IEEE Transactions on Geoscience and Remote Sensing*, *37*(2 II), 987–999. https://doi.org/10.1109/36.752217

Pinty, B., Lavergne, T., Widlowski, J. L., Gobron, N., & Verstraete, M. M. (2009). On the need to observe vegetation canopies in the near-infrared to estimate visible light absorption. *Remote Sensing of Environment*, *113*(1), 10–23. https://doi.org/10.1016/j.rse.2008.08.017

Savill, P., Perrins, C., Kirby, K., & Fisher, N. (2011). Wytham Woods: Oxford's ecological laboratory. https://doi.org/10.1093/acprof:osobl/9780199605187.001.0001

Schneider, F. D., Leiterer, R., Morsdorf, F., Gastellu-Etchegorry, J. P., Lauret, N., Pfeifer, N., & Schaepman, M. E. (2014). Simulating imaging spectrometer data: 3D forest modeling based on LiDAR and in situ data. *Remote Sensing of Environment*, *152*, 235–250. https://doi.org/10.1016/j.rse.2014.06.015

Soma, M., Pimont, F., Durrieu, S., & Dupuy, J. L. (2018). Enhanced measurements of leaf area density with T-LiDAR: Evaluating and calibrating the effects of vegetation heterogeneity and scanner properties. *Remote Sensing*, *10*(10), 1580. https://doi.org/10.3390/rs10101580

Stuckens, J., Somers, B., Delalieux, S., Verstraeten, W. W., & Coppin, P. (2009). The impact of common assumptions on canopy radiative transfer simulations: A case study in Citrus orchards. *Journal of Quantitative Spectroscopy and Radiative Transfer*, *110*(1–2), 1–21. https://doi.org/10.1016/j.jqsrt.2008.09.001

Thome, K. J. (2001). Absolute radiometric calibration of Landsat 7 ETM+ using the reflectance-based method. *Remote Sensing of Environment*, *78*(1–2), 27–38. https://doi.org/10.1016/S0034-4257(01)00247-4

Thome, K. J., Arai, K., Tsuchida, S., & Biggar, S. F. (2008). Vicarious calibration of ASTER via the reflectance-based approach. *IEEE Transactions on Geoscience and Remote Sensing*, *46*, 3285–3295. https://doi.org/10.1109/TGRS.2008.928730

Ünsalan, C., & Boyer, K. L. (2004). Linearized vegetation indices based on a formal statistical framework. *IEEE Transactions on Geoscience and Remote Sensing*, *42*(7), 1575–1585. https://doi.org/10.1109/TGRS.2004.826787

Van der Zande, D., Stuckens, J., Verstraeten, W. W., Mereu, S., Muys, B., & Coppin, P. (2011). 3D modeling of light interception in heterogeneous forest canopies using ground-based LiDAR data. *International Journal of Applied Earth Observation and Geoinformation*, *13*(5), 792–800. https://doi.org/10.1016/j.jag.2011.05.005

Verhoef, W. (1984). Light scattering by leaf layers with application to canopy reflectance modeling: The SAIL model. *Remote Sensing of Environment*, *16*(2), 125–141. https://doi.org/10.1016/0034-4257(84)90057-9

Verhoef, W., & Bach, H. (2007). Coupled soil-leaf-canopy and atmosphere radiative transfer modeling to simulate hyperspectral multi-angular surface reflectance and TOA radiance data. *Remote Sensing of Environment*, *109*(2), 166–182. https://doi.org/10.1016/j.rse.2006.12.013

Vicari, M. B., Pisek, J., & Disney, M. (2019). New estimates of leaf angle distribution from terrestrial LiDAR: Comparison with measured and modelled estimates from nine broadleaf tree species. *Agricultural and Forest Meteorology*, *264*, 322–333. https://doi.org/10.1016/j.agrformet.2018.10.021

Vincent, G., Antin, C., Laurans, M., Heurtebize, J., Durrieu, S., Lavalley, C., & Dauzat, J. (2017). Mapping plant area index of tropical evergreen forest by airborne laser scanning. A cross-validation study using LAI2200 optical sensor. *Remote Sensing of Environment*, *198*, 254–266. https://doi.org/10.1016/j.rse.2017.05.034

Wang, Y., Czapla-Myers, J., Lyapustin, A., Thome, K., & Dutton, E. G. (2011). AERONET-based surface reflectance validation network (ASRVN) data evaluation: Case study for railroad valley calibration site. *Remote Sensing of Environment*, *115*(10), 2710–2717. https://doi.org/10.1016/j.rse.2011.06.011

Weber, J., & Penn, J. (1995). Creation and rendering of realistic trees. *Proceedings of the ACM SIGGRAPH Conference on Computer Graphics*. https://doi.org/10.1145/218380.218427

Weiser, H., Winiwarter, L., Anders, K., Fassnacht, F. E., & Höfle, B. (2021). Opaque voxel-based tree models for virtual laser scanning in forestry applications. *Remote Sensing of Environment*, *265*, 112641. https://doi.org/10.1016/j.rse.2021.112641

Widlowski, J. L., CÔté, J. F., & Béland, M. (2014). Abstract tree crowns in 3D radiative transfer models: Impact on simulated open-canopy reflectances. *Remote Sensing of Environment*, *142*, 155–175. https://doi.org/10.1016/j.rse.2013.11.016

Widlowski, J. L., Mio, C., Disney, M., Adams, J., Andredakis, I., Atzberger, C., et al. (2015). The fourth phase of the radiative transfer model intercomparison (RAMI) exercise: Actual canopy scenarios and conformity testing. *Remote Sensing of Environment*, *169*, 418–437. https://doi.org/10.1016/j.rse.2015.08.016

Widlowski, J. L., Pinty, B., Lopatka, M., Atzberger, C., Buzica, D., Chelle, M., et al. (2013). The fourth radiation transfer model intercomparison (RAMI-IV): Proficiency testing of canopy reflectance models with ISO-13528. *Journal of Geophysical Research: Atmospheres*, *118*(13), 6869–6890. https://doi.org/10.1002/jgrd.50497

Woodgate, W., Disney, M., Armston, J. D., Jones, S. D., Suarez, L., Hill, M. J., et al. (2015). An improved theoretical model of canopy gap probability for Leaf Area Index estimation in woody ecosystems. *Forest Ecology and Management*, *358*, 303–320. https://doi.org/10.1016/j.foreco.2015.09.030



21698996, 2022, 14, Downloaded from https://agupubs.onlinelibrary.wiley.com/doi/10.1029/2021JD036175 by Portail BibCNRS INSU, Wiley Online Library on [16/03/2023]. See the Terms and Conditions (https://onlinelibrary.wiley.com/terms-and-conditions) on Wiley Online Library for rules of use; OA articles are governed by the applicable Creative Commons License